science.sciencemag.org/cgi/content/full/science.abe6523/DC1

Supplementary Materials for

RNA stabilization by a poly(A) tail 3′-end binding pocket and other modes of poly(A)-RNA interaction

Seyed-Fakhreddin Torabi, Anand T. Vaidya, Kazimierz T. Tycowski, Suzanne J. DeGregorio, Jimin Wang, Mei-Di Shu, Thomas A. Steitz, Joan A. Steitz*

*Corresponding author. Email: joan.steitz@yale.edu

Published 7 January 2021 on *Science* First Release
DOI: 10.1126/science.abe6523

This PDF file includes:

Other supplementary material for this manuscript includes:

MDAR Reproducibility Checklist (PDF)

Supplementary Text

Crystallization

Initial native gel shift assays performed to evaluate TWIFB1 dENE binding affinity to poly(A) of different lengths were carried out using a poly(A) RNA ladder generated by partial alkali digestion of longer poly(A) RNAs (Sigma). This study was conducted to identify a proper range for poly(A) length to be tested in crystallization trials. Poly(A) fragments of different lengths were purified by denaturing PAGE and then ^{32}P 5′-end radiolabeled. It is known that the 3′ end of RNA fragments generated by alkali hydrolysis contains a 2′,3′-cyclic phosphate and is stable at neutral pH (*49*). Poly(A) of different lengths used in crystallization trials were chemically synthesized and therefore end with 3′-OH group. Later, after determining the crystal structure of the Xtal dENE+poly(A)$_{28}$ complex, we realized that poly(A) with a 2′,3′-cyclic phosphate is predicted to create a steric clash with the backbone of the pocket motif. As described in the Results section, the presence of the 2′,3′-cyclic phosphate reduces the dENE's binding affinity for poly(A) and results in an ~2-fold increase in K_d.

Co-crystallization trials were conducted using more than 40 RNA sequence variants complexed with poly(A) of different lengths ranging from 25 to 30 nt. All crystallization dENE constructs contained the same dENE core sequence (Fig. 1A) but varied the sequence outside the dENE core, e.g. different length and/or composition of the flanking regions. We also tested the wild-type dENE by removing its 5-nt single-stranded 5′ and 3′ flanking regions (Fig. 1A), which did not yield diffraction-quality crystals. Except for the wild-type crystallization constructs, all others contained a hairpin structure with a GAAA tetraloop located either on top of the upper dENE domain or the bottom of the lower dENE domain. To evaluate conformational homogeneity of the dENE+poly(A) complexes, native gel analysis was carried out. As shown in fig. S4, the poly(A)-bound Xtal dENE complex prepared for crystallization trials showed that a conformationally homogeneous complex crystalizes.

The stabilization activity of the Xtal dENE was tested using an intronless β-globin mRNA reporter assay. We speculate that the longer upper stem and thereby formation of extra minor-groove interactions in the Xtal dENE might be responsible for observing higher accumulation of the β-globin transcript compared to the wild-type dENE.

A poly(A) 3′-end binding pocket composed solely of RNA that facilitates formation of a blunt-ended triple helix

The dENE+poly(A)$_{28}$ structure reveals tight packing of the 3′-most adenosine of poly(A) in the pocket motif. We performed EMSAs using several dENE and poly(A) variants to evaluate the impact of creating steric clash between poly(A) 3′ end and the pocket motif. Addition of a single G to the 3′ end of poly(A)$_{28}$, which is predicted to induce a steric clash with the dENE G33 phosphate, weakens the binding of dENE to poly(A) by an ~2-fold increase in K_d (fig. S16). Furthermore, a significant smear forms below the complex band (fig. S16B). The smear was resolved when a double-mutant dENE, M25, which sequesters the 3′-G overhang into the major-groove triple helix through formation of a C-G•C$^+$ base triple, was used in the assay (fig. S16A, B and D). In addition, we compered the binding affinity of two poly(A) substrates containing an internal G substitution (poly(A)$_{25}$G(A)$_2$ and poly(A)$_{25}$G(A)$_4$) to another double-mutant dENE, M26, with two U to C mutations in the middle of the lower dENE domain (fig. S18A). Earlier studies showed that such ENE mutants were able to locate a single G in a stretch of A nucleotides, form a C-G•C$^+$ base triple, and thereby lock the register of poly(A) binding (*11, 17*). When bound

to M26, poly(A)$_{25}$G(A)$_2$ is expected to form a blunt-ended triplex, while poly(A)$_{25}$G(A)$_4$ should generate a 2-nt overhang of the 3′ end of poly(A), predicting steric clash with the pocket motif (fig. S17). Our data show that the predicted steric clash results in an ~3-fold reduction in the binding affinity (fig. S17B and C).

The M26 dENE contains a double U to C mutation in the lower dENE domain. This mutant is expected to lock the poly(A) register through formation of a C-G•C$^+$ triple and to leave a 20-nt long poly(A) 3′ overhang (*11, 17*). The deadenylation assay of M26 dENE demonstrates that the 20-nt poly(A) 3′ overhang is rapidly trimmed away and no further deadenylation occurs beyond that point (Fig. 4D).

In the pocket motif, CUC/GAG base pairing is close to 100% conserved in dENEs (fig. S2), although the corresponding stem in single domain ENEs (fig. S22) does not show such high sequence conservation. Based on the dENE crystal structure, the G33, A34 and G35 nucleotides occupy positions that poly(A) would occupy if the poly(A) strand were computationally extended using the geometry of the last three A nucleotides in the dENE+poly(A)$_{28}$ crystal structure. Purine nucleotides at the G33, A34 and G35 positions stack well with poly(A) bases. Moreover, the G33-C59 closing base pair is more thermodynamically favorable than the weaker Watson-Crick interaction of an A-U base pair. In addition, the G35-C57 base pair is highly conserved as it is hydrogen bonded to N1 of A31. However, based on our current crystal structure, we cannot explain why the A34-U58 is highly conserved in dENEs.

Formation of the pocket motif through interactions between the adenosine triad and the major groove of the double-helical stem into which the triad inserts augment sequestration of the poly(A) tail by protecting its very 3′ end. “Hiding” the 3′-most adenosine of the poly(A) tail in a pocket-containing ENE is a stabilization mechanism distinct from those of elements that impede exonuclease activities through a ‘roadblock’ mechanism (*50-54*). Since RNA 3′-end accessibility and processing play fundamental roles in the stability and cellular fate of RNA transcripts (*55-59*), protecting the poly(A) 3′ end through formation a blunt-ended RNA triplex is a powerful mechanism to regulate RNA stability and, potentially, activity.

Finally, the TWIFB1 dENE structure reveals that dENE+poly(A) is a modular assembly. Specifically, the pocket motif appears to exist in several ENEs despite different modes of interaction with poly(A) in the minor groove or of how poly(A) transitions to the major-groove triple helix (figs. S2 and S22). Therefore, the repertory of identified ENEs (*9*) represents different combinations of various types of structural modules.

Significance of dENE+poly(A) structural features in RNA stabilization

The upper and lower domains of the dENE share several common structural features, i.e. WC/H A-minor interactions, the quintuple-base transition and major-groove triple helix. Our cellular assays demonstrated that identical mutations are more detrimental to the cellular level of βΔ1,2 reporter transcript when in the upper compared to the lower dENE domain. For example, mutating the C-G base pair in the quintuple base transition in the upper domain (M1) reduces the accumulation of β-globin mRNA to ~38%, while the same mutation in the lower domain (M3) results in ~48% activity compared to the wild-type dENE. Since the presence of the poly(A) 3′-end pocket is the major difference between the two domains, we hypothesize that the pocket motif compensates for mutations that disrupt other features of the lower domain. If this hypothesis is true, a mutation that affects both the lower domain major groove triple helix and the pocket motif should result in greater activity loss in the reporter assay. For example, the U to C mutation in M18

is expected to disrupt the major-groove triple helix, while also compromising the proper arrangement the 3′-most adenosine of poly(A) and its ability to form a hydrogen bond with the G33 phosphate within the backbone of the pocket. Indeed, M18 shows the least activity (~30%) among mutations tested in the lower dENE domain.

The greater detrimental effects observed for mutations in the upper domain on the stabilization activity of dENE in the reporter assay might be explained by kinetic effects. We speculate that the upper dENE domain might bind poly(A) first, as previously proposed (*9*), and thus assist the lower dENE domain in searching for the poly(A) 3′ end and docking it into the pocket motif. Since the poly(A) register is not fixed in the upper dENE domain and its 3′ end can freely exit the upper major-groove triple helix, we hypothesize that poly(A) can easily slide out of the upper domain and loop out variable numbers of nucleotides between the two dENE domains. Further investigations are required to shed light on the folding and dynamics of dENE-poly(A) complex formation.

The crystal structure reveals a structural reason for the frequent occurrence of a G•A pair closing the upper dENE domain in multiple dENEs (fig. S2). In M9, which replaces the non-canonical G74•A14 base pair with a G-C pair, we observed ~40% reduction in stabilization activity, consistent with our previous data (*9*). Although G•A is an antiparallel pair that can be extended into a canonical double-helical stem, it is less stable than a GC canonical pair (*60*). Based on the structure, although A15, which emerges from the upper dENE major-groove triple helix, does not interact with the G74•A14 base pair (figs. S9 and S19B), poly(A) A14 forms a stacking interaction with the adenine of the G74•A14 base pair (fig. S19); therefore, mutating A14 in the dENE to C should disrupt the stacking interaction.

Conservation of pyrimidine/purine (Y/R) bias in the composition of the flanking stems that form WC/H A-minor interactions supports the importance of this feature in dENE function. In the upper stem, all four base pairs are involved in WC/H A-minor interactions. In the crystal structure, the top three base pairs provide a landing pad for poly(A) in the minor groove, while the CG closing base pair is involved in the quintuple transition motif. In the M21 mutant, the dENE upper stem and hairpin are replaced with GCUUCGGC, a thermodynamically stable tetraloop that is not known to bind any particular protein or make RNA-RNA interactions (*61, 62*). Disruption of the WC/H A-minor motif in M21 showed ~60% reduction in the accumulation of the reporter transcript, comparable to M2 (Fig. 5). To address the significance of Y/R bias in each receptor base pair, we mutated A-U to U-A in M22, A-U to U-A in M23, and C-G to G-C in M24 (fig. S20). M23 and M24, which exhibit less Y/R bias in the upper stem, showed lower activity. In contrast, M22 with higher Y/R bias increased the RNA stabilization activity of the dENE by ~20%. In the PAN or MALAT1 ENE, whose poly(A) or A-rich tract forms only a few classical A-minor interactions with the flanking stem, only mutation of the closing base pair results in lower stabilization activity (~50%); mutating any other base pair in the stem to another canonical pair has no significant effect on RNA stabilization (*7, 12*). These observations agree with earlier studies showing that A-minor interactions do not differ among canonical receptor base pairs (*63, 64*). However, WC/H A-minor interactions in the dENE appear to prefer a particular geometry, as well as Y/R bias in the composition of the stems. Yet, we cannot rule out the possibility that protein interactors recognize this feature in vivo.

The canonical A-minor motif is one of the most abundant tertiary interactions found in numerous RNA structures (*18, 65*). Canonical A-minor interactions include four subtypes based on the positioning of the adenosine in the minor groove and the number of hydrogen bonds it forms

(type 0, I, II and III). The number of consecutive adenosines in a canonical A-minor motif does not exceed three (*18, 64*). When three consecutive adenosines are involved, the interactions conform to a type order as follows: the 5′-most adenosine forms a type III, the middle A forms a type II, and the 3′-most adenosine makes a type I interaction. This particular structural topology precludes involvement of more than three consecutive adenosines (*18, 64*). The majority of interactions that the GAAA tetraloop-minor groove receptor forms are canonical A-minor interactions (*66-68*) and they also occur in the PAN and MALAT1 triplex structures (*11, 17*). In contrast, a tract of more than three consecutive adenosines can form a WC/H A-minor motif by interacting with a Y/R biased stem. Therefore, WC/H A-minor motifs have the potential to form stable interactions with RNA double helices and are expected to play an important role in stabilization of polyadenylated RNAs.

Until this study, formation of a blunt-ended triplex structure was identified only by locking the register of A-rich tracts using its non-A nucleotides. Previous studies demonstrated that superior activity of the MALAT1 ENE in stabilizing RNA is due to the formation of a blunt-ended triplex (*7, 17*). Similarly, a mutated PAN ENE, which generates a blunt-ended RNA triplex locked into the register by substituting one U-A•U with a C-G•C^+ triple, is as active as MALAT1 in inhibiting rapid RNA decay (*17*). We inserted the TWIFB1 dENE or PAN ENE upstream of a 54- or 72-mer poly(A) tract in the reporter plasmid and compared their activities with a reporter containing the MALAT1 ENE and A-rich tract in the same position (fig. S21A). The βΔ1,2-dENE-poly$(A)_{54}$ or -poly$(A)_{72}$ exhibits an increase in accumulation of the reporter transcript that is closer to that of MALAT1, but higher than those of ENEs that do not form blunt-ended triplex structures (PAN ENE or Δpocket dENE mutants) (fig. S21B and C). Therefore, the pocket motif facilitates formation of a blunt-ended RNA triplex without relying on the presence of non-A nucleotides in the poly(A) tail.

Based on our current knowledge, dENEs are found in transposable elements, predominantly in plants and fungi. Median poly(A) tail lengths in plants (< 100 nt (*69*)) and fungi (~60 nt (*70*)) are less than those in mammalian cells (~35% and ~65%, respectively, compared to HEK293T cells (*71, 72*)). Therefore, structural features of dENEs might have evolved to stabilize poly(A) tails of ~60–120-nt long most efficiently. This is in agreement with our observation that TWIFB1 dENE stabilizes the βΔ1,2 reporter transcript more effectively when its poly(A) tail is ~70 nt long (fig. S21).

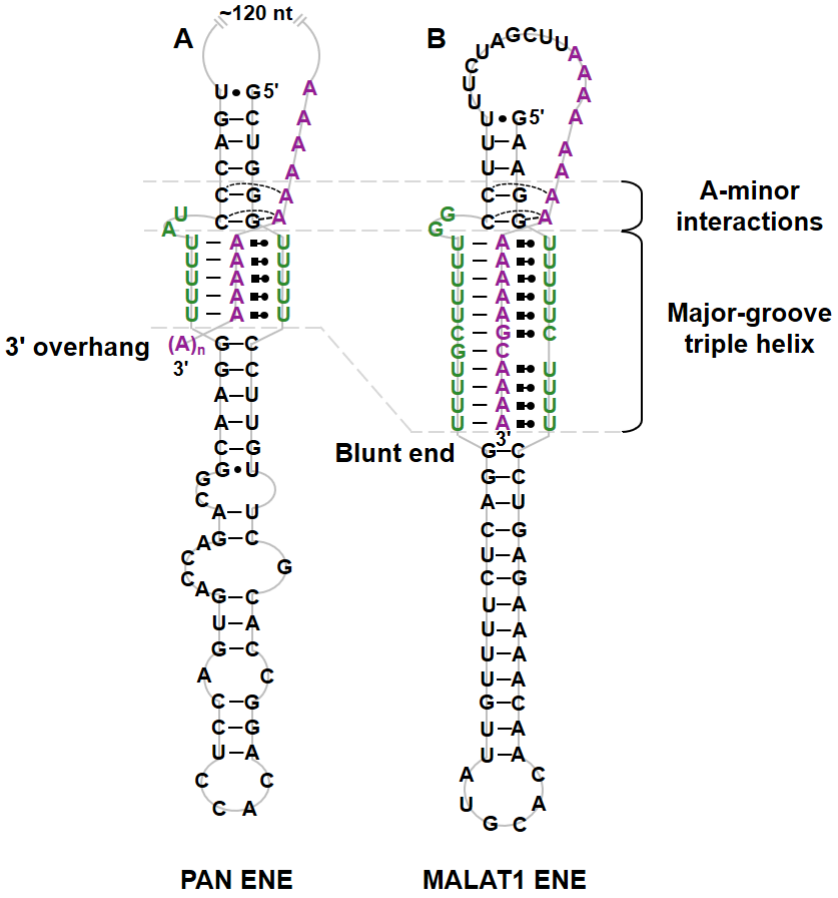

Fig. S1. Schematic diagram of the triple helical structure of the PAN RNA (crystal structure at 2.5 Å resolution) (*11*) (A) and the MALAT1 (crystal structure at 3.1 Å resolution) (*17*) (B) ENEs. URILs (U-rich internal loops) are shown in green; the poly(A) tail and A-rich tract are in purple. The upside-down representation of PAN RNA and MALAT1 ENEs is presented for easier comparison with the TWIFB1 dENE.

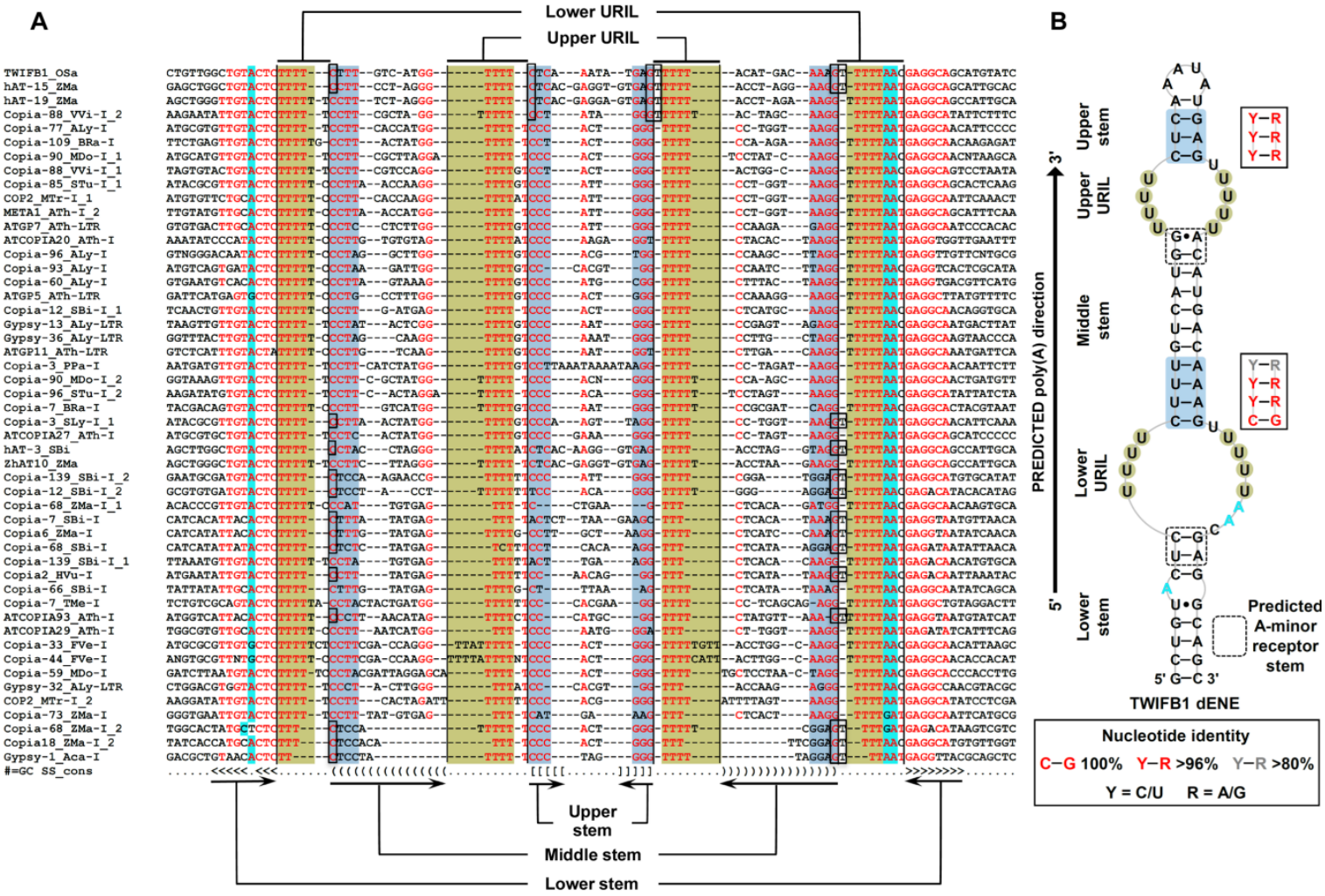

Fig. S2. Sequence conservation of dENEs. (A) Secondary structure-guided alignment of TE sequences corresponding to dENEs and their flanking regions, described in (*9*). The Ts specifying the U residues involved in predicted U-A•U triple-helix formation in dENE are shaded green, while pyrimidine/purine (Y/R) biased stems are shaded blue. The three conserved adenosines constituting the adenosine triad are shaded cyan. Residues involved in the quintuple-base transition, a motif found in the TWIFB1 dENE+poly(A)$_{28}$ complex, are boxed. Red residues are at least 60% conserved. **(B)** Predicted secondary structure of the rice TWIFB1 dENE. Colors are as in A. The black arrow indicates the predicted 5′ to 3′ direction of the poly(A) interacting with the dENE based on structural homology with the PAN and MALAT1 ENEs. The consensus structures of the Y/R biased stems, derived from the sequence alignment shown in (A), are depicted in black boxes on the right.

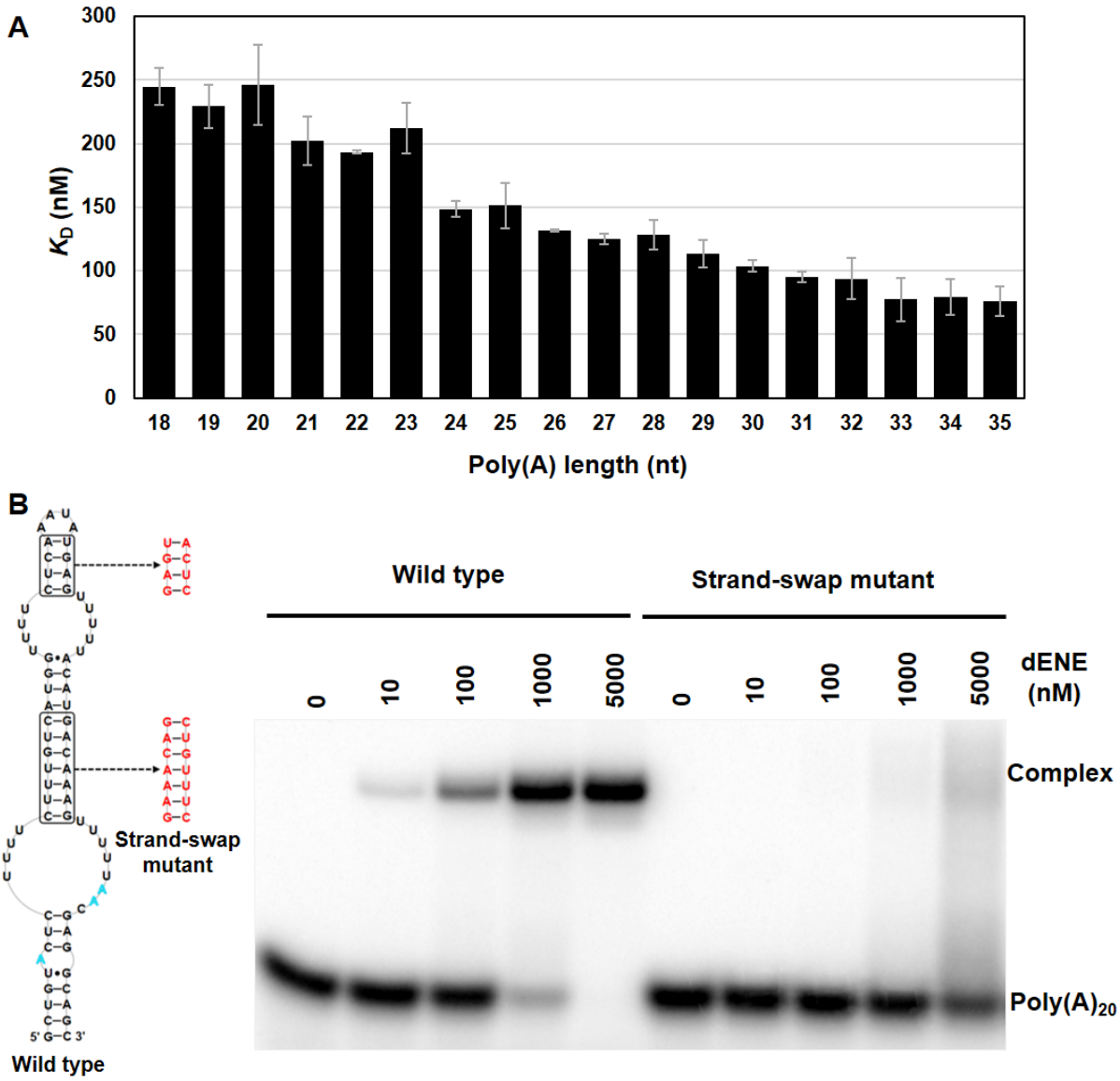

Fig. S3. Interactions between poly(A) RNAs and the dENE investigated using native gel shift assays. (A) Binding affinities of the wild-type dENE shown in (B) for poly(A) of different lengths (18 to 35 mers) were investigated. Poly(A) fragments were generated by partial alkali hydrolysis of poly(A) (Sigma) followed by PAGE purification. For each poly(A) length, native gel shift assays with trace [^{32}P] 5′-end labeled poly(A) were carried out. Binding affinities are the average of at least three replicates ± standard deviation. **(B)** The contribution of the Y/R biased stems to the ability of the dENE to bind poly(A) was evaluated using native gel shift assays. The strand-swap mutation, in which both Y/R biased stems were strand-swapped (red nucleotides), obliterated poly(A)-binding.

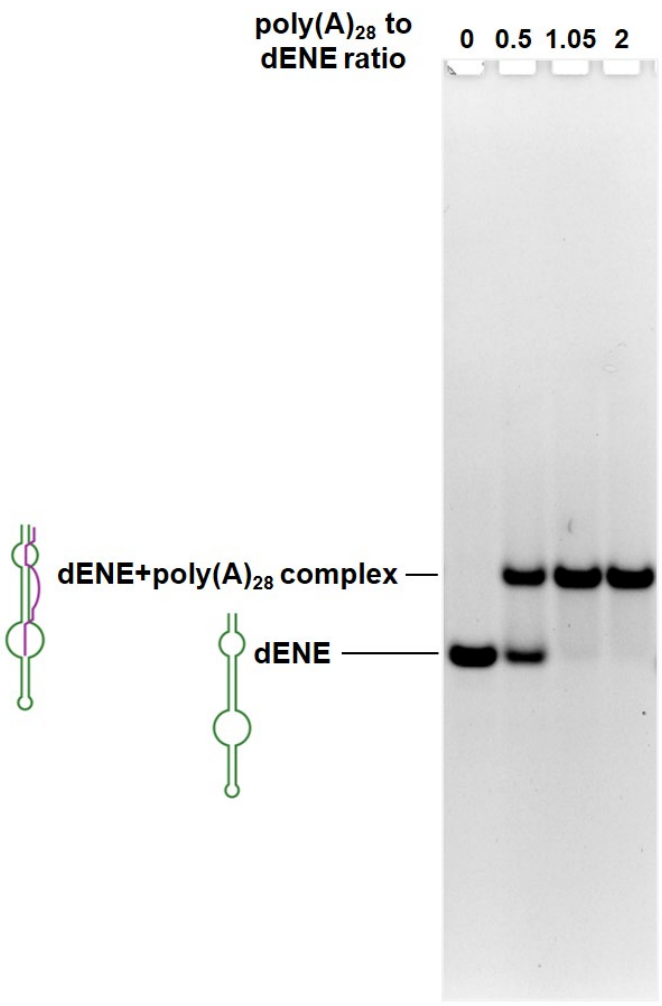

Fig. S4. Evaluation of the purity and homogeneity of the Xtal dENE+poly(A)$_{28}$ complex prepared for crystallization trials using native gel electrophoresis. Xtal RNA (~5.7 mg/ml or ~170 µM) was mixed with poly(A)$_{28}$ in different molar ratios, heated to 95 °C for 2.5 min, snap-cooled on ice for 10 min, then equilibrated to room temperature over 1 h. RNA was visualized by ethidium bromide staining.

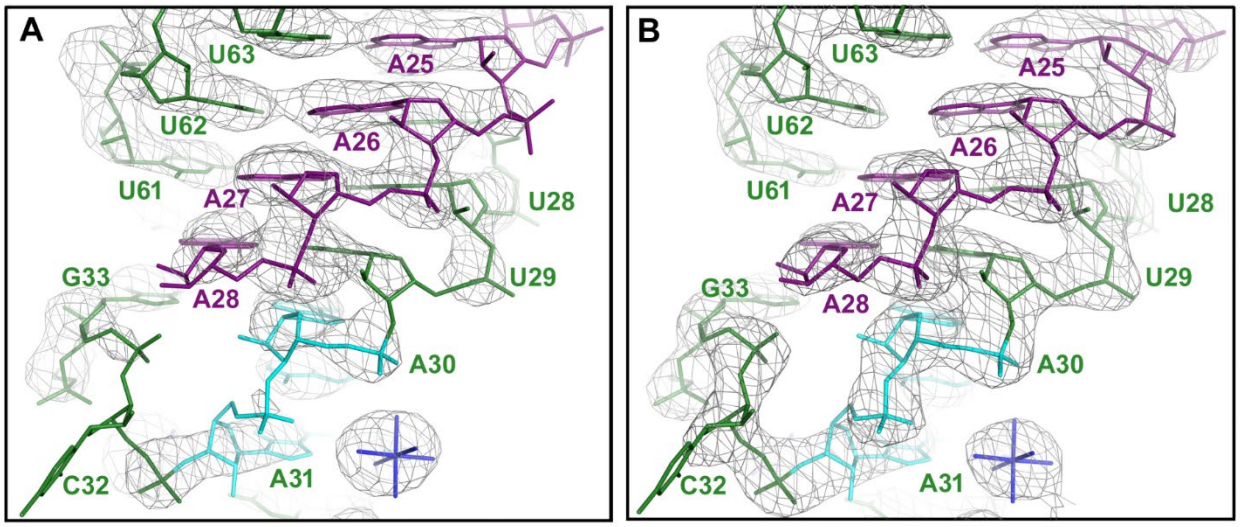

Fig. S5. Representative electron density maps. Initial experimental electron density for a portion of the complex including the poly(A) 3′-end binding pocket at 3.10-Å resolution, contoured at 2σ **(A)**, and the final $2F_o - F_c$ electron density for the same region at 2.89-Å resolution, contoured at 2σ **(B)**. Colors as in Fig. 1. An iridium hexamine ion, which is bound to the RNA backbone, is shown in blue.

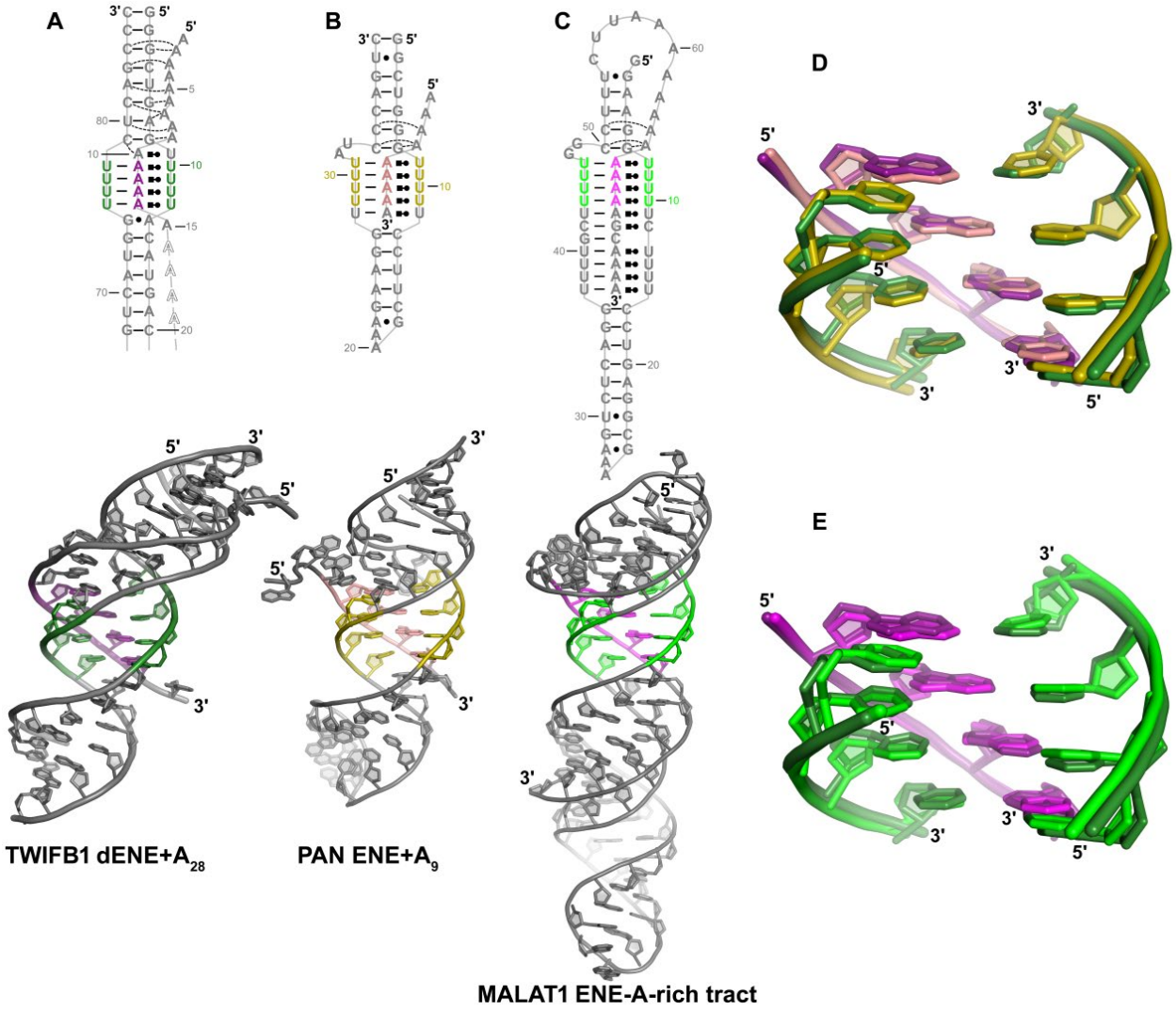

Fig. S6. Three different ENEs form identical major-groove triple helices with poly(A). Schematic diagrams of the triple helix structure (above) and cartoon representation (below) of the crystal structures of the TWIFB1 upper domain **(A)**, PAN RNA **(B)**, and MALAT1 **(C)** ENEs. Superposition of the major-groove triple helix (colored regions) from the TWIFB1 upper domain with the major-groove triple helix from PAN RNA (RMSD = 0.8 Å) **(D)** or MALAT1 (RMSD = 0.8 Å) **(E)**. Colors and orientations are as in (A to C). The PAN and MALAT1 triplex structures were derived from PDB 3P22 (*11*) and 4PLX (*17*), respectively.

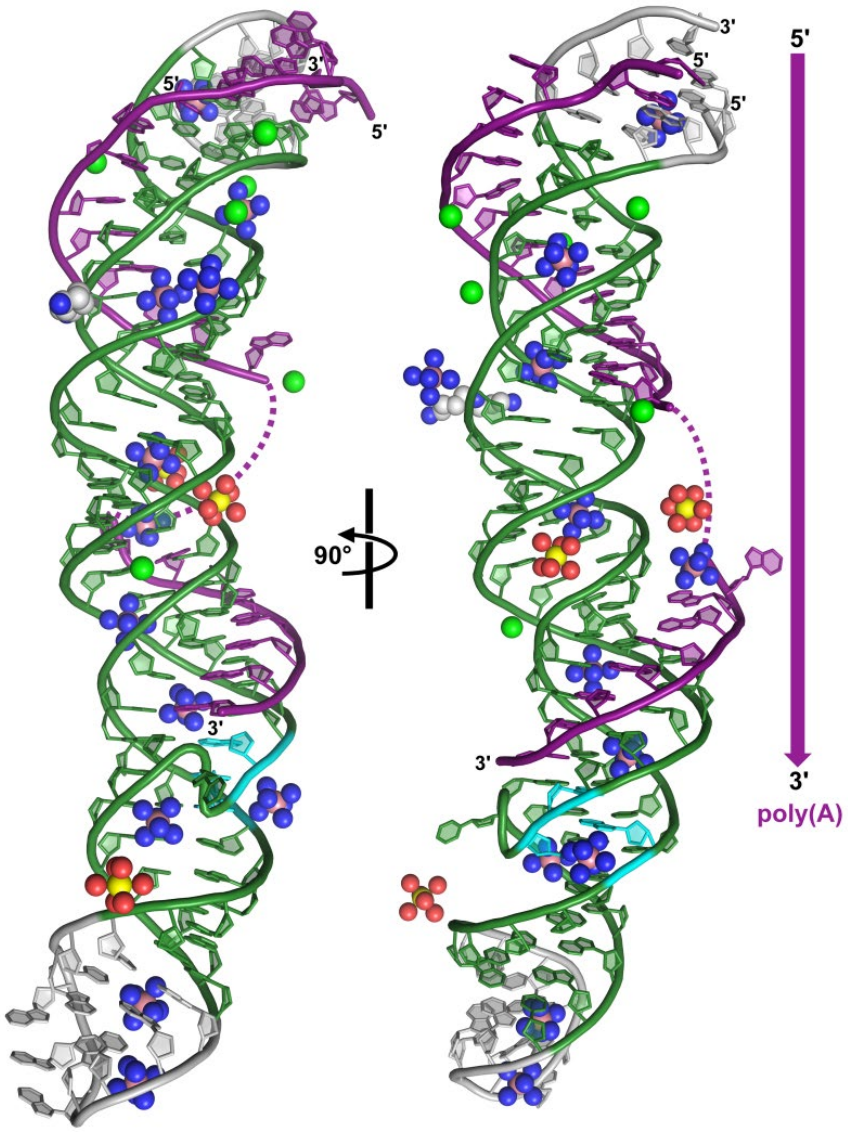

Fig. S7. Overall structure of the Xtal dENE+poly(A)$_{28}$ complex in the same views as shown in Fig. 1E. Additionally shown are eleven iridium hexamine ions (salmon surrounded by blue spheres), six strontium ions (green spheres), three magnesium hexahydrate ions (yellow surrounded by red spheres) and a single spermidine (white complexed with blue spheres) that are bound to the complex. The 5′ to 3′ direction of poly(A) interaction with the upper and then the lower dENE domain is shown by a purple arrow.

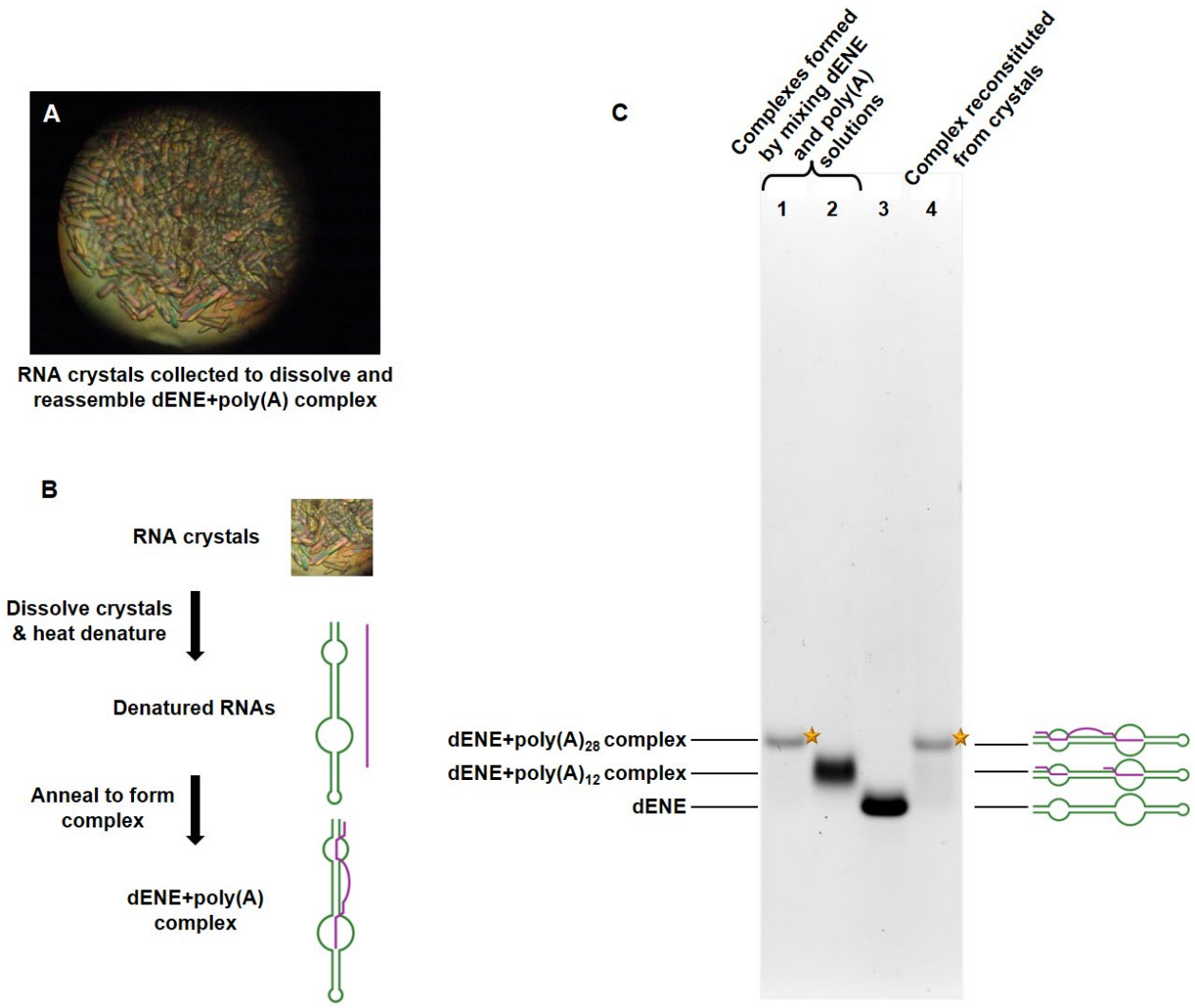

Fig. S8. Analysis of the Xtal dENE+poly(A)$_{28}$ complex reconstituted from dissolved RNA crystals using a native gel mobility shift assay. RNA crystals from multiple drops **(A)** were dissolved to reconstitute the dENE+poly(A)$_{28}$ complex **(B)** and then analyzed by mobility shift relative to free dENE on a native gel later stained with ethidium bromide **(C)**. RNA samples were heat denatured at 95 °C for 3 min and then cooled to room temperature for 1 h. dENE+poly(A)$_{28}$ and dENE+poly(A)$_{12}$ complexes, lanes 1 and 2, were formed by mixing dENE:poly(A) in a 1:1.05 and 1:2.1 ratio, respectively. RNA crystals collected from multiple drops (A) were washed with mother liquor solution ten times to remove all soluble RNA, then dissolved in 1 mM $MgCl_2$ containing buffer, heat denatured and annealed using the above protocol and loaded in lane 4. The RNA in lane 1 is the dENE+poly(A)$_{28}$ complex used as the starting material to set up crystallization trays. Observing the same mobility shift (marked by orange stars) in lane 1 for the complex assembled before crystallization and lane 4 (the complex reconstituted from RNA retrieved from crystals after releasing poly(A) by heat denaturation) indicates that poly(A)$_{28}$ in the crystal remains intact. Therefore, the lack of electron density for A_{16}-A_{20} in the X-ray structure appears to not result from poly(A) scission; the A_{16}-A_{20} region is most likely crystallographically disordered.

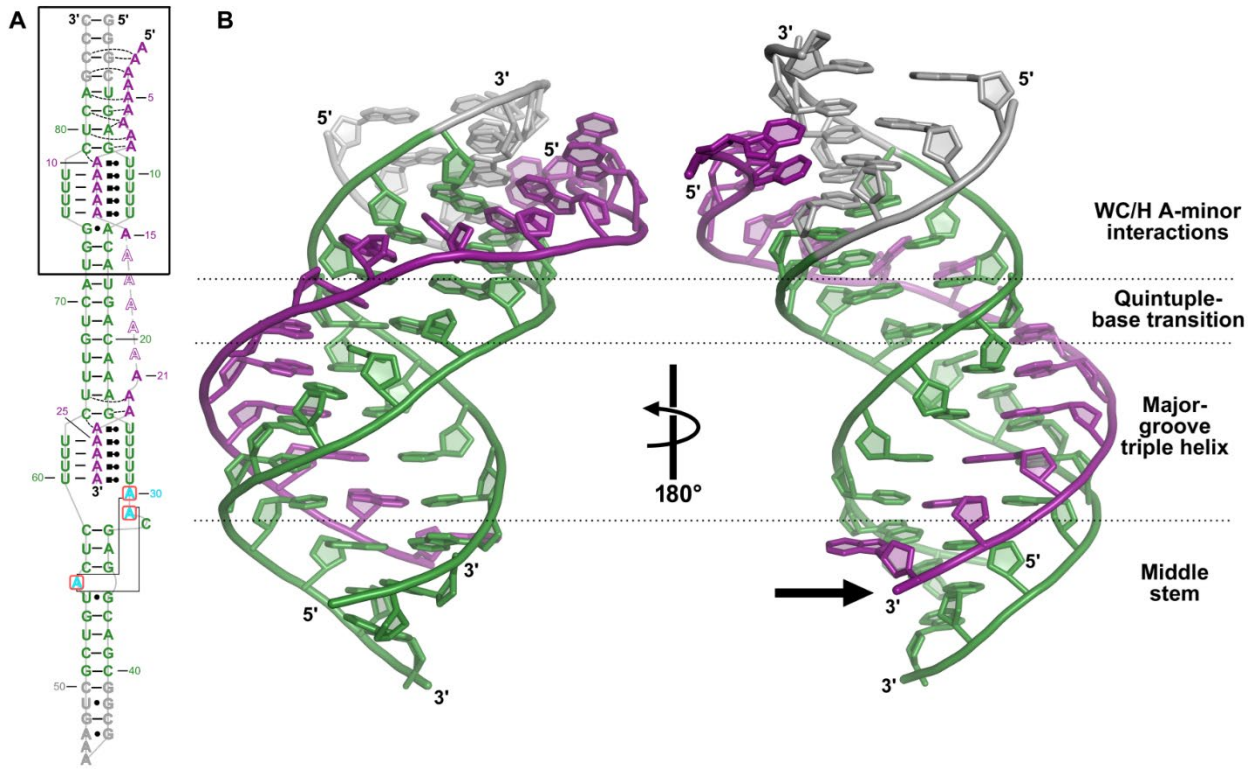

Fig. S9. Structural features of the upper dENE domain in the Xtal dENE+poly(A)$_{28}$ complex. **(A)** Schematic diagram of the tertiary structure of the entire dENE+poly(A)$_{28}$ complex as shown in Fig. 1. **(B)** Cartoon representation of the structure of the upper domain boxed in (A). Poly(A) lies in the minor groove of the upper stem, making multiple WC/H A-minor interactions. In the quintuple-base transition motif, poly(A) shifts from the WC/H A-minor motif to form a major-groove triple helix. The first A to emerge from the major-groove triple helix, A15, points its 3′-O away from the middle stem (black arrow).

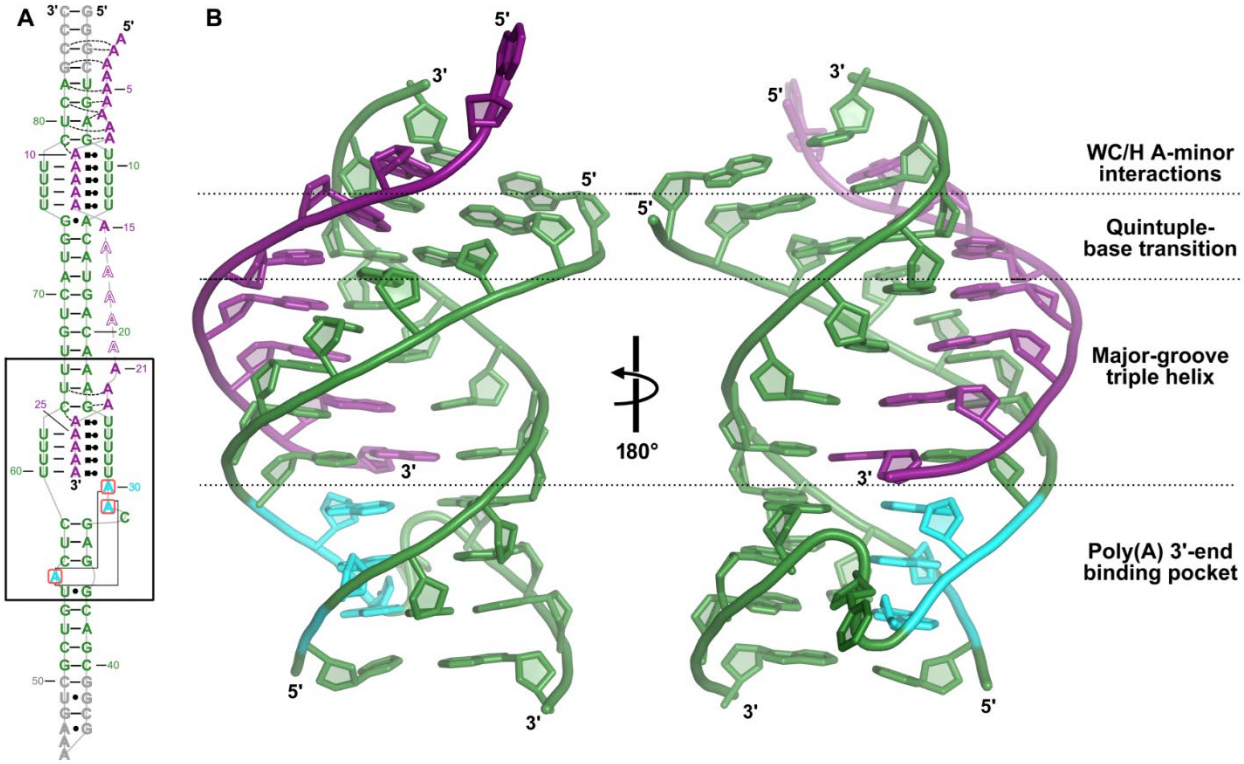

Fig. S10. Structural organization of the lower dENE domain in the Xtal dENE+poly(A)$_{28}$ complex. (A) Schematic representation of the tertiary structure of the entire dENE+poly(A)$_{28}$ complex. **(B)** Cartoon representation of the structure of the lower domain boxed in (A). A22 of poly(A) interacts with the minor groove of the middle stem. Through the quintuple-base transition, poly(A) shifts from a WC/H A-minor interaction to form a major-groove triple helix. The poly(A) 3′ end is buried in the pocket motif formed by stacking interactions between the adenosine triad bases (cyan), which insert into the major groove of the three base pairs of the stem flanking the lower URIL.

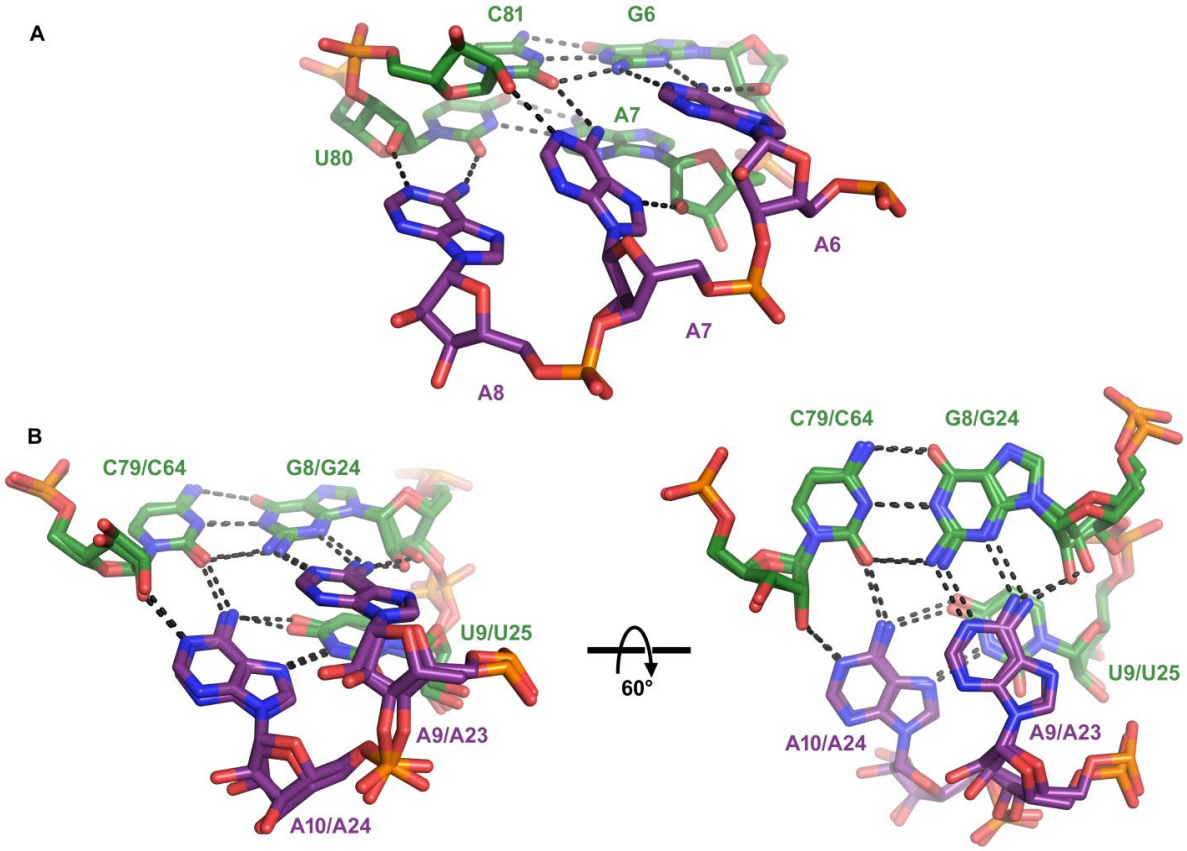

Fig. S11. Base triple and base quintuple interactions observed in the Xtal dENE+poly(A)$_{28}$ structure. (A) A7 of poly(A) hydrogen bonds with two adjacent base pairs (U80-A7 and C81-G6) in a twisted conformation to form a quintuple-nucleotide interaction. The same base pairs also participate in two triple-base interactions: A6 with C81-G6 and A8 with U80-A7. **(B)** The quintuple-base transition motifs between WC/H A-minor interactions and major-groove triple helices are identical in the upper and lower dENE domains: superposition of the two quintuple-base transition motifs is shown in two different views (RMSD = 0.7 Å over all non-hydrogen atoms).

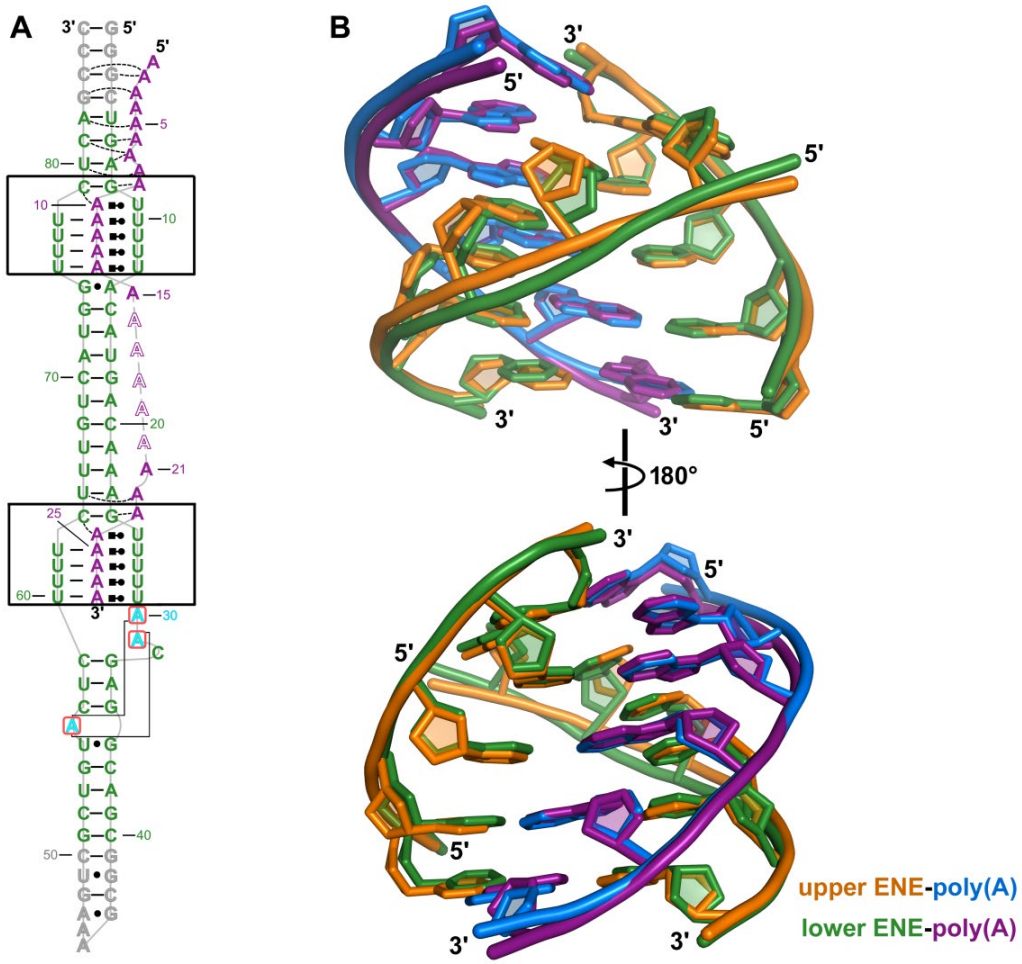

Fig. S12. Structurally identical quintuple-base transitions and major-groove triple helices form in the upper and lower dENE domains. (A) Schematic diagram of the complex tertiary structure. **(B)** Superposition of the two regions boxed in (A) is shown in two different views (RMSD = 0.8 Å over all nonhydrogen atoms).

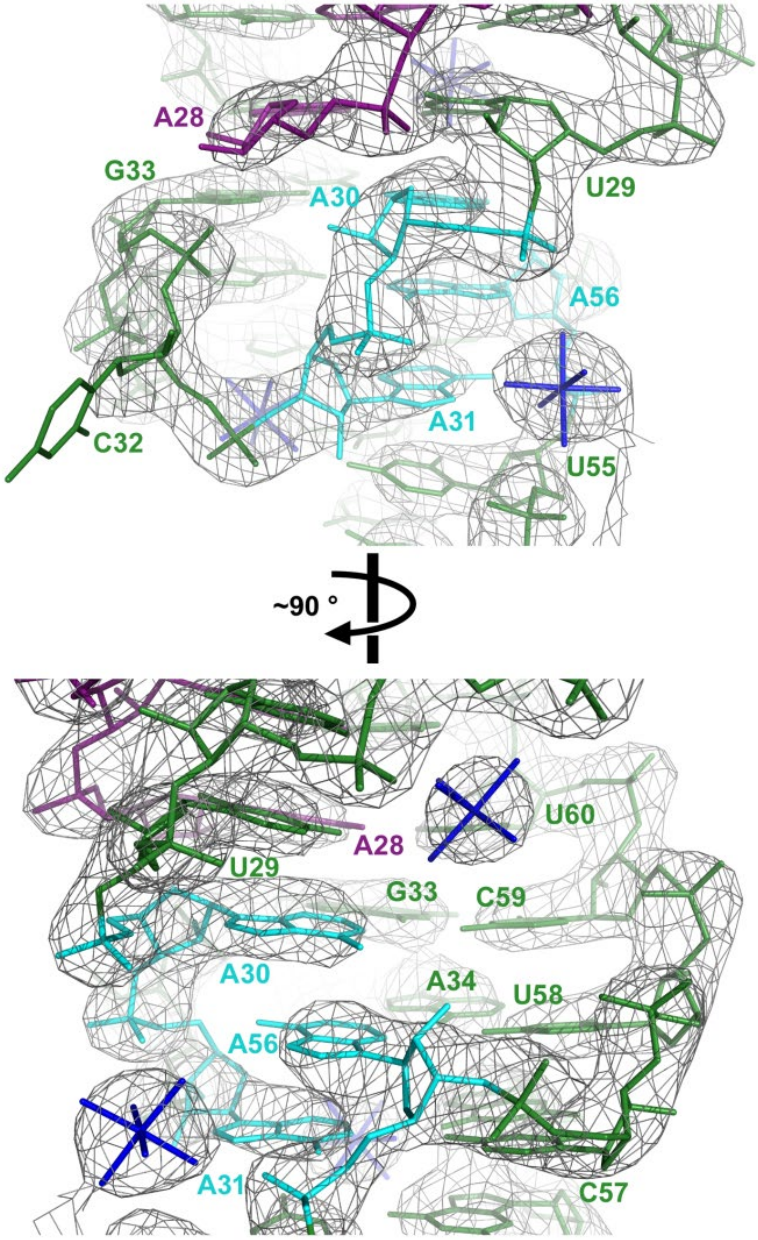

Fig. S13. Final electron density for the adenosine triad in the poly(A) 3′-end binding pocket contoured at 2σ. Colors as in Fig. 1. Iridium hexamine ions, which are bound to the RNA backbone, are shown in blue.

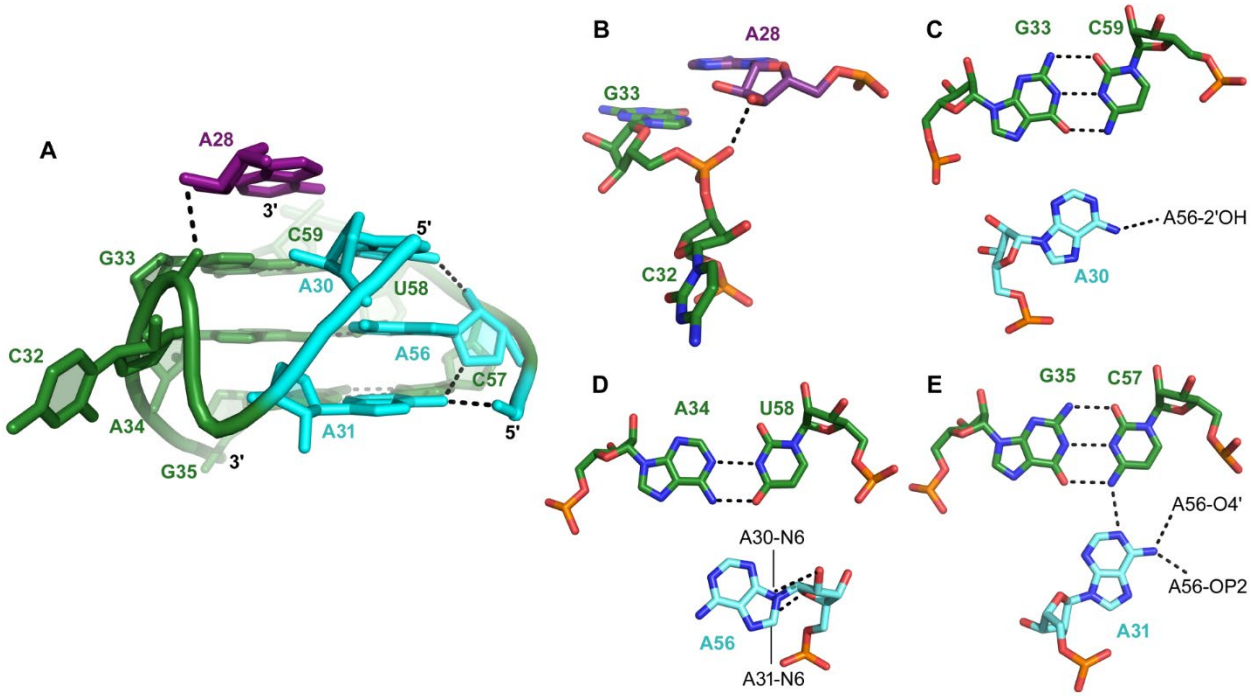

Fig. S14. The hydrogen-bond network formed in the poly(A) 3′-end binding pocket. (A) A30, A56 and A31, which form base-stacking interactions, reside in the major groove of three base pairs of the stem located next to the lower URIL. The A30, A56 and A31 bases are coplanar with the C59-G33, U58-A34 and C57-G35 base pairs, respectively. The base C32 in the middle of the Z-shaped backbone positions the G33 phosphate within hydrogen-bonding distance of the terminal 3′-OH group of poly(A)$_{28}$ **(B)**. **(C to E)** Close-up and top views of the interactions between the adenosine triad and base pairs forming the flanking double helix.

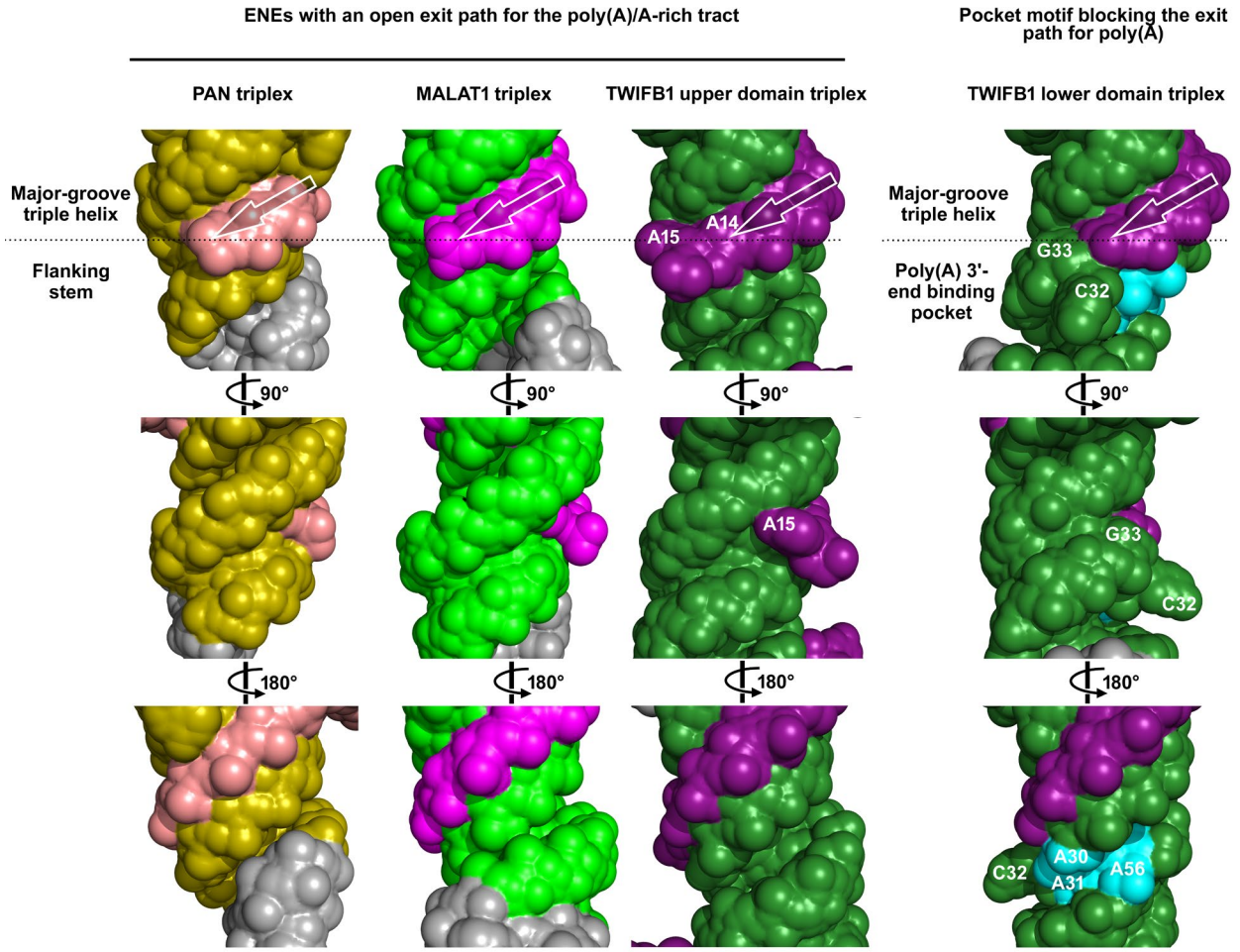

Fig. S15. Molecular surface representations of the triplex structures from different ENEs, which expand Fig. 4A (top row) by presenting two other orientations (the middle and bottom rows). The 90° rotations reveal the 3′-most adenosine of each triplex, which faces the wide and shallow minor groove of the flanking stem. In the TWIFB1 upper dENE domain, the A15 nucleotide emerges from the major-groove triplex. In contrast to the other three triple helices, in the TWIFB1 lower dENE triplex, the entrance to the minor groove of the flanking stem is closed and the groove is narrowed and more shallow. The 180° rotations show the narrow and deep major grooves of the flanking stems. Unlike the first three structures, in the TWIFB1 lower dENE triplex, which is flanked by the poly(A) 3′-end binding pocket, the depth of the major groove is filled by the adenosine triad. The PAN and MALAT1 structures were derived from PDB 3P22 and 4PLX, respectively.

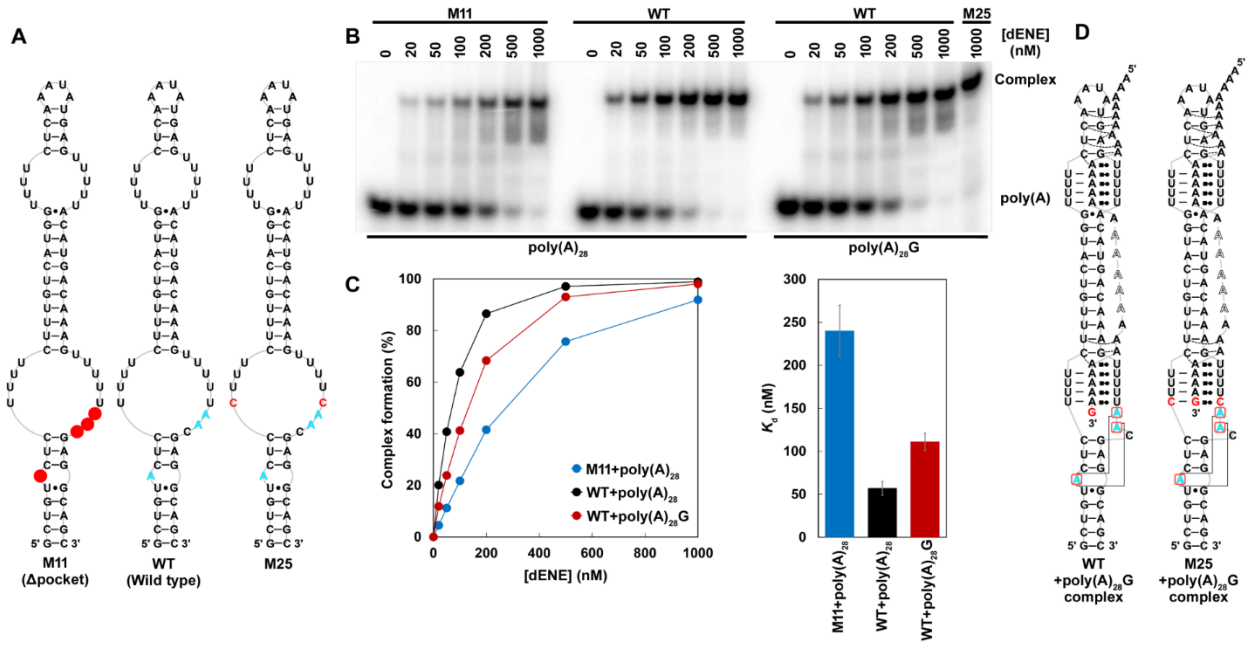

Fig. S16. Native gel shift assays support the importance of the pocket motif for dENE function. Binding affinities of various dENE constructs for [^{32}P]-5′-end labeled poly(A)$_{28}$ and poly(A)$_{28}$G were investigated using EMSA. **(A)** Predicted secondary structures of tested dENE constructs. Mutated nucleotides are in red and deleted ones are marked by red circles. **(B)** Native gel shift assays of the WT or mutated dENE as indicated at the top with poly(A)$_{28}$ or poly(A)$_{28}$G as marked at the bottom. Disruption of the poly(A) 3′-end binding pocket by deleting residues critical for the formation of the pocket (in M11) or by introducing a steric clash between a nucleotide leaving the major-groove triple helix (single G in poly(A)$_{28}$G) and phosphate backbone of the pocket results in 1) appearance of a smear below the complex band (B), and 2) reduction in the binding affinity **(C)**. In M25, the double U to C mutation, which should engage G of poly(A)$_{28}$G in formation of a C-G•C^{+} triple and thereby eliminate the steric clash, resolves the smear (last lane of B). Binding affinities are the average of at least three replicates ± standard deviation. **(D)** Predicted interactions of the dENE constructs used in the assay with poly(A)$_{28}$G.

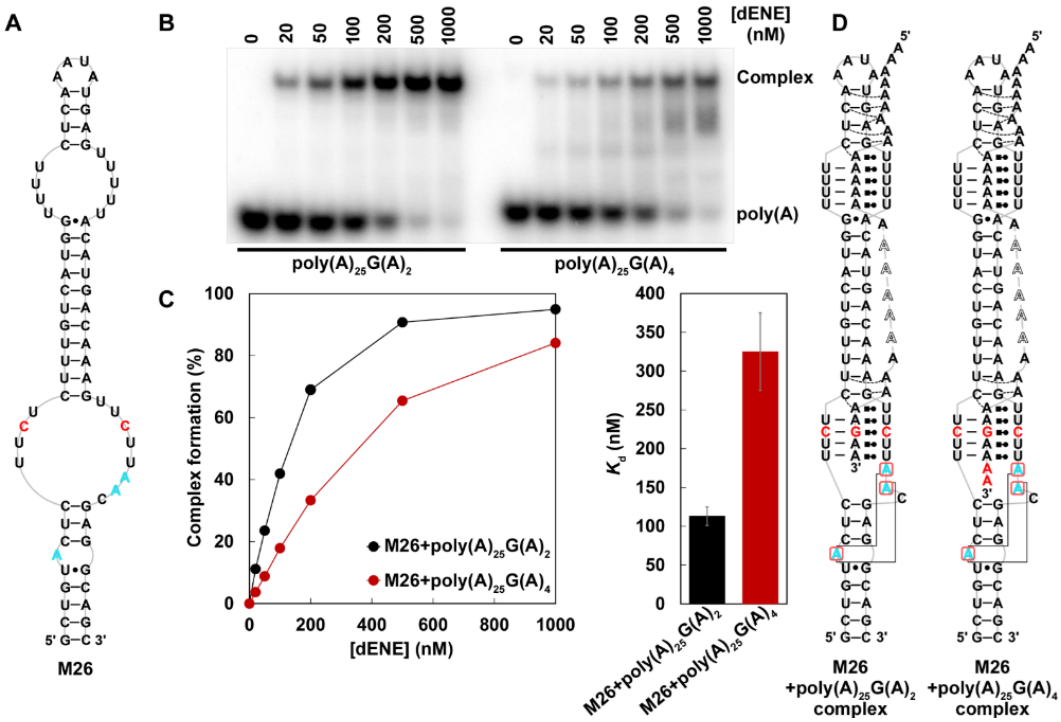

Fig. S17. Native gel shift assays support formation of the pocket through a steric mechanism. Binding affinity of a dENE construct with a double U to C mutation in the middle of the lower dENE domain for G-containing poly(A) sequences was investigated by EMSA. **(A)** Predicted secondary structure of the double-mutant construct used in the assay. Mutated nucleotides are in red. **(B)** Native gel shift assays of M26 with poly(A)$_{25}$G(A)$_2$ or with poly(A)$_{25}$G(A)$_4$. The introduction of a steric clash between the two nucleotides leaving major-groove triple helix (two As) and the phosphate backbone of the pocket results in 1) appearance of a smear below the complex band (B), and 2) a reduction in binding affinity **(C)**. Binding affinities are the average of at least three replicates ± standard deviation. **(D)** Predicted interaction of the M26 double-mutant dENE with poly(A)$_{25}$G(A)$_2$ or poly(A)$_{25}$G(A)$_4$.

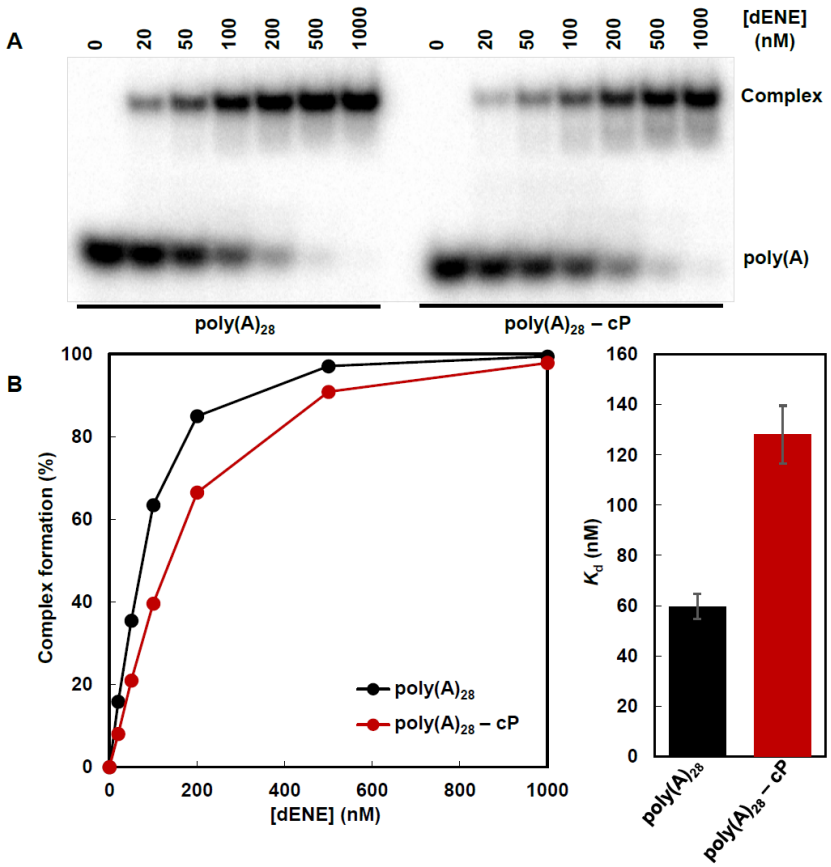

Fig. S18. The effect of replacing the 3′-OH group in poly(A) with 2′, 3′-cyclic phosphate on binding to the dENE. (A) Native gel shift assays of complexes formed between the dENE and poly(A)$_{28}$ terminating with either 3′-OH [poly(A)$_{28}$] or 2′, 3′-cyclic phosphate [poly(A)$_{28}$-cP]. **(B)** Quantification of the samples shown in (A). Binding affinities are the average of at least three replicates ± standard deviation.

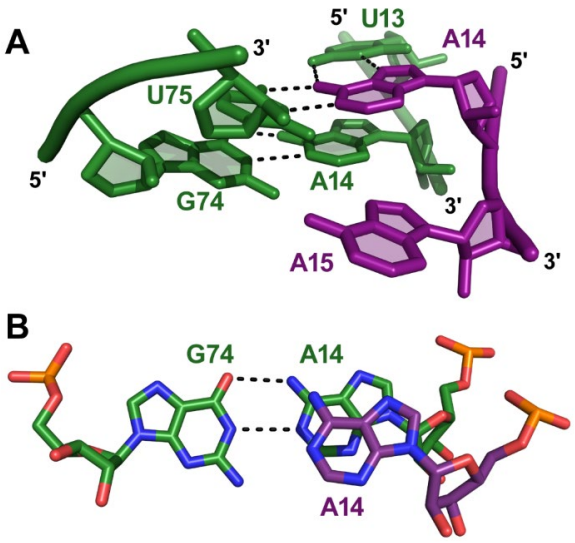

Fig. S19. Stacking interaction between A14 of poly(A) and the adenine of the G74•A14 base pair of the dENE. (A) Close-up and side view of the G74•A14 base pair located next to the last U-A•U triple in the upper dENE domain. **(B)** Top view of the stacking interaction between A14 of poly(A) and the A14 of the dENE.

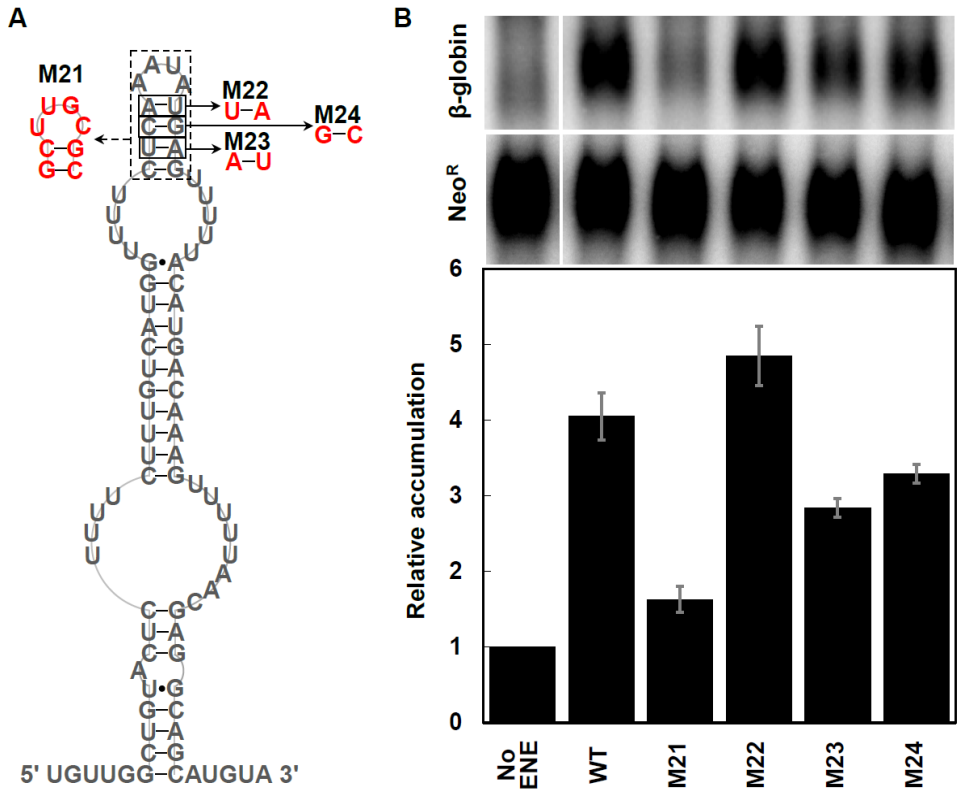

Fig. S20. Contribution of WC/H A-minor interactions to the accumulation of the β-globin reporter mRNA. (A) Predicted secondary structure of the dENE with the mutations studied in the assay indicated. Gray is the wild-type sequence while mutated nucleotides are red. **(B)** Northern blots probed for β-globin and neomycin resistance (Neo^R) sequences. For quantification of the Northern blot results, the β-globin signals were normalized to those of Neo^R. Accumulation of No ENE was set at 1. Relative accumulation is the average of at least three independent experiments ± standard deviation.

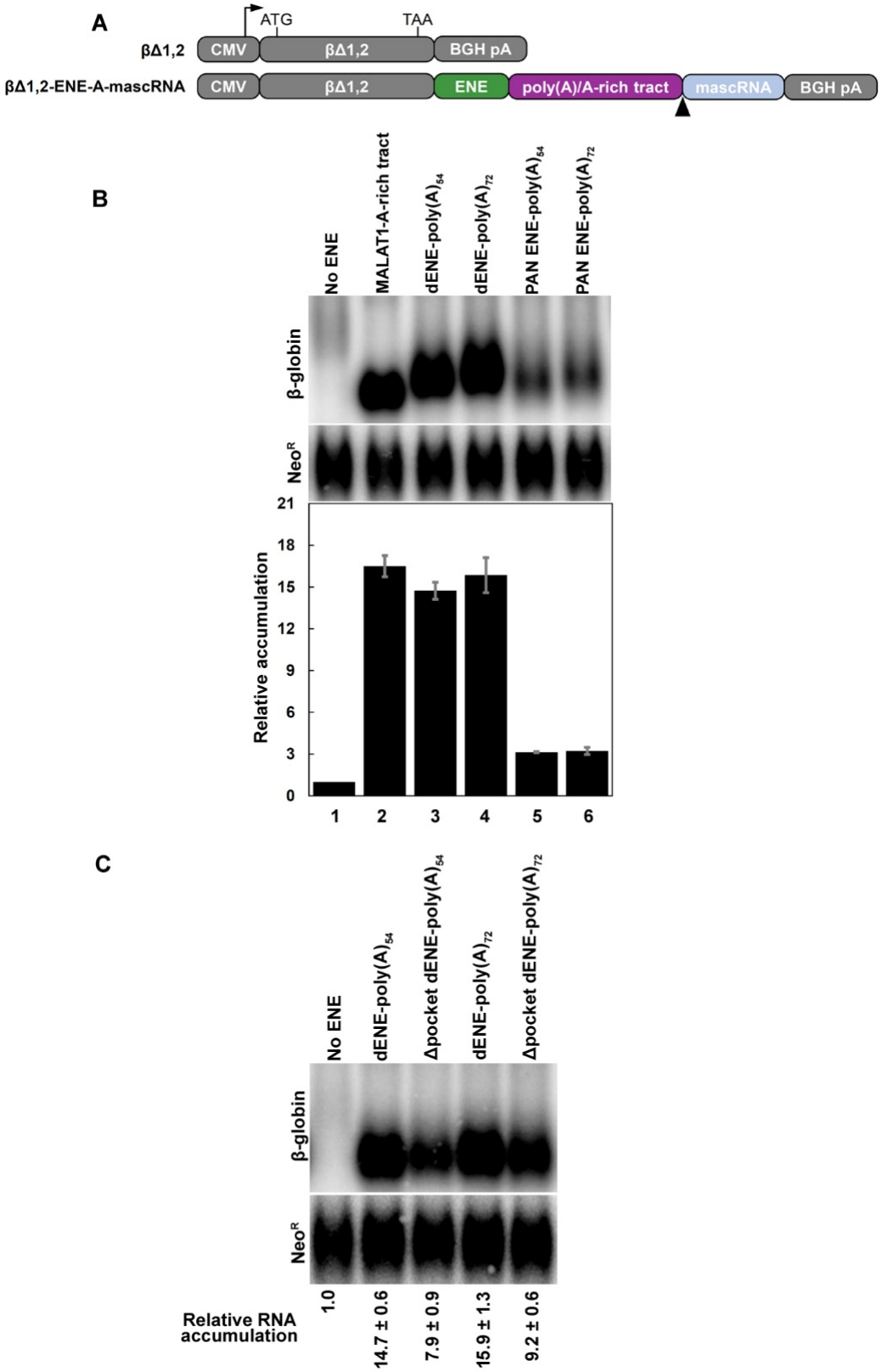

Fig. S21. Comparative accumulation of β-globin reporter transcripts containing different ENEs. Accumulation of β-globin reporter transcripts stabilized by ENEs forming 3′-blunt ended

triple helices (TWIFB1 dENE and MALAT1 ENE) or ENEs that do not form 3′-blunt ended triplex structures (PAN ENE and Δpocket dENE) are investigated. **(A)** Schematic of the β-globin constructs containing a CMV promoter, a human intronless β-globin gene (βΔ1,2), different ENEs, poly(A)/A-rich tract, mascRNA and a bovine growth hormone poly(A) site (BGH pA). Arrowhead indicates the RNase P cleavage site upstream of mascRNA. **(B)** Northern blot analyses of different β-globin reporter constructs. Blots (top) were probed for β-globin and neomycin resistance (Neo^R) sequences. Quantification of the Northern blots (bottom) with the β-globin signals normalized to those of Neo^R. **(C)** Removal of the poly(A) 3′-end binding pocket from the same constructs as used in (B) results in reduction of RNA accumulation by ~50%. Relative accumulation of No ENE was set at 1. Relative accumulation is the average of at least three independent experiments ± standard deviation.

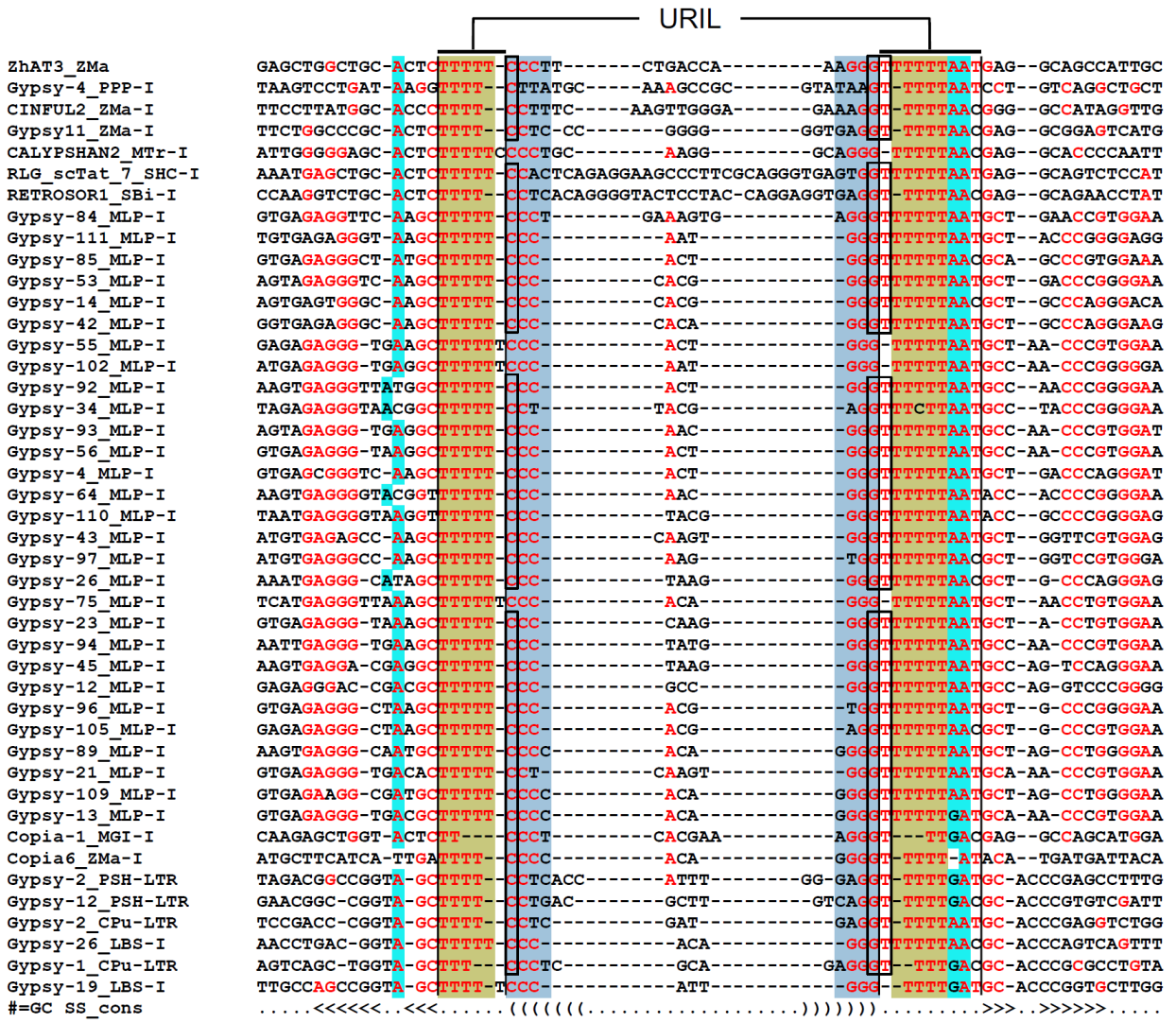

Fig. S22. Secondary structure-guided alignment of TE sequences corresponding to single-domain ENEs and their flanking regions, described in (*9*). Residues putatively involved in the quintuple-base transition are boxed, while the three conserved adenosines constituting the adenosine triad, which is involved in poly(A) 3′-end binding pocket formation, are shaded cyan. The Ts specifying the U residues involved in predicted U-A•U triple-helix formation by the ENE are shaded green, while pyrimidine/purine (Y/R) biased stems are shaded blue. The red residues are at least 60% conserved.

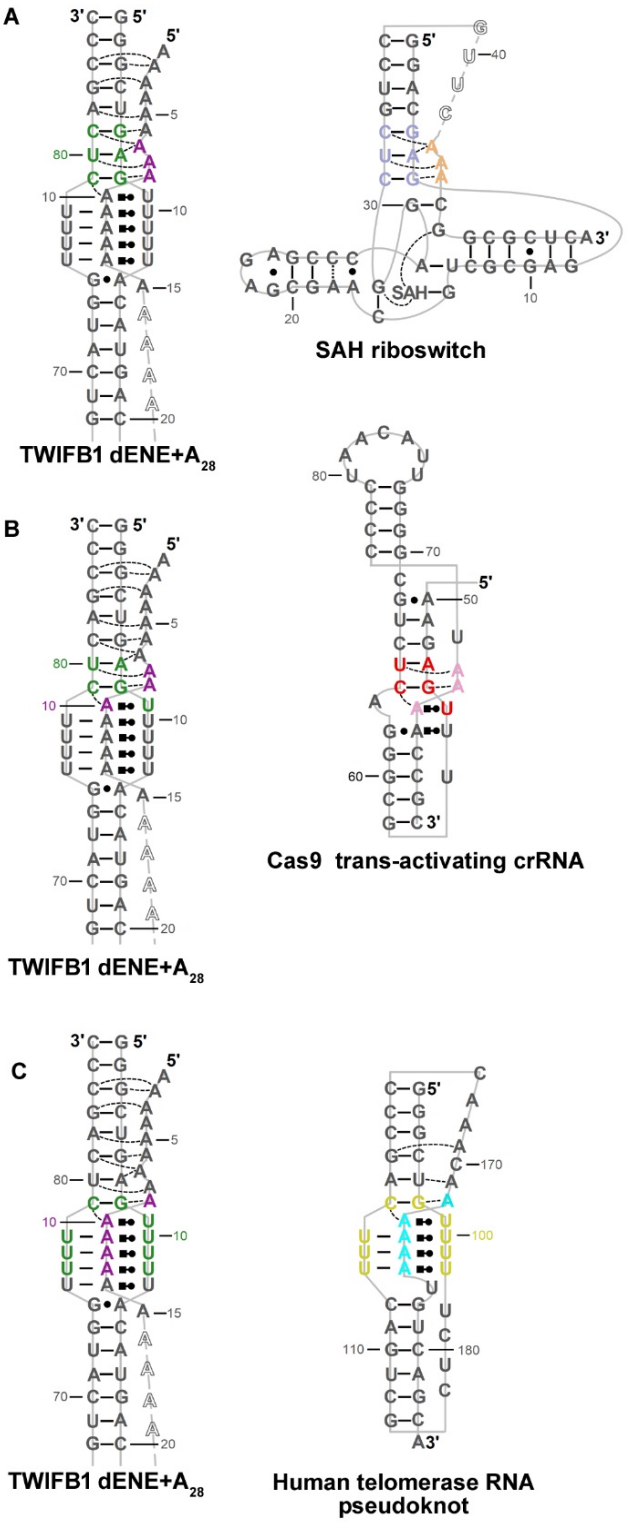

Fig. S23. Schematic diagrams of the structures used for superposition analyses in Fig. 6. Only those regions used for superposition are colored. **(A)** Schematic diagrams of dENE+poly(A)$_{28}$ and the SAH riboswitch (*20*). **(B)** Schematic diagrams of dENE+poly(A)$_{28}$ and the Cas9 trans-activating crRNA (*21*). **(C)** Schematic diagrams of the dENE+poly(A)$_{28}$ complex and the hTR pseudoknot (*22*).

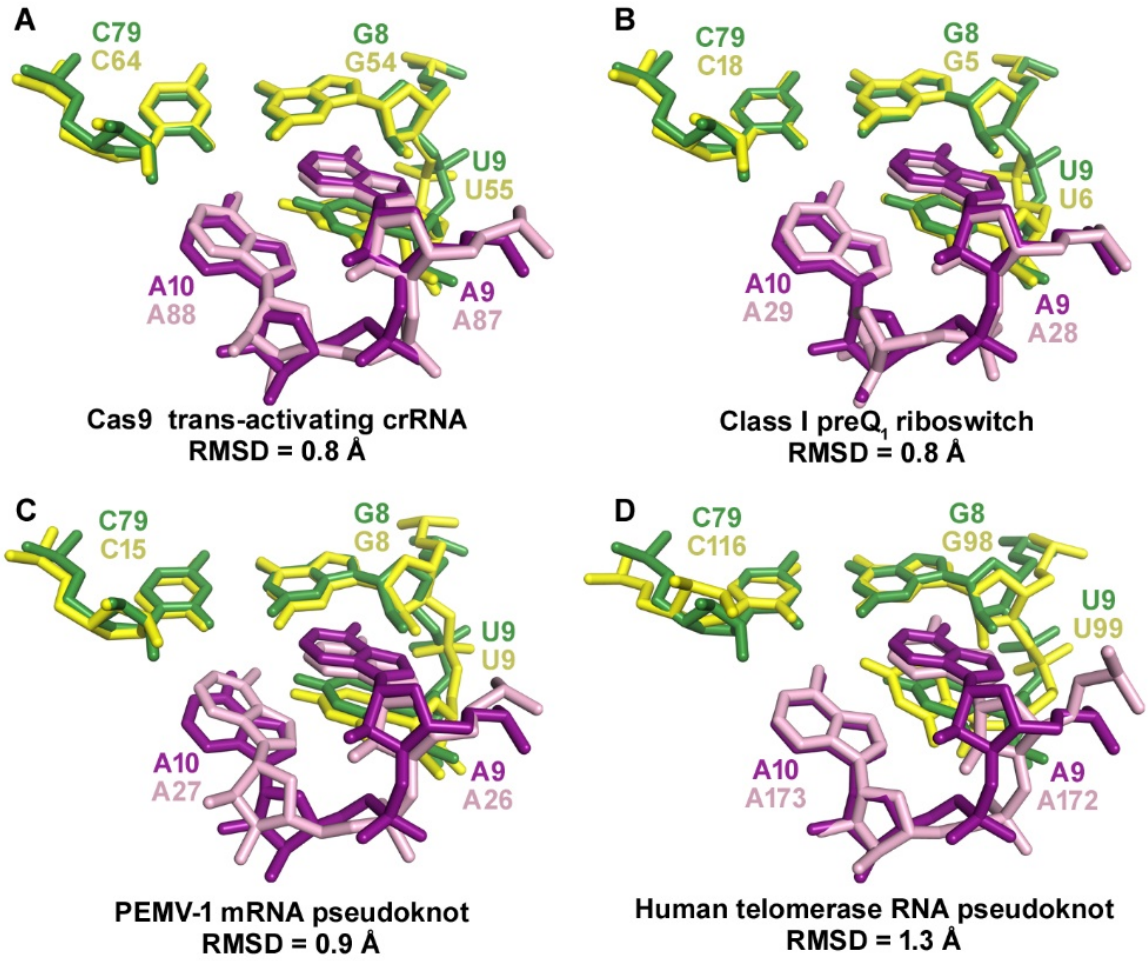

Fig. S24. Comparison of the quintuple-base transition motifs from different RNA structures. The quintuple-base transition motif from the dENE+poly(A)$_{28}$ structure is superimposed on that of **(A)** the Cas9 trans-activating crRNA (PDB 5X2G (*21*)), **(B)** the Class I preQ1 riboswitch (PDB 3FU2 (*24*)), **(C)** the PEMV-1 mRNA pseudoknot (PDB 2RP0 (*73*)), or **(D)** the hTR pseudoknot (PDB 2K95 (*22*)).

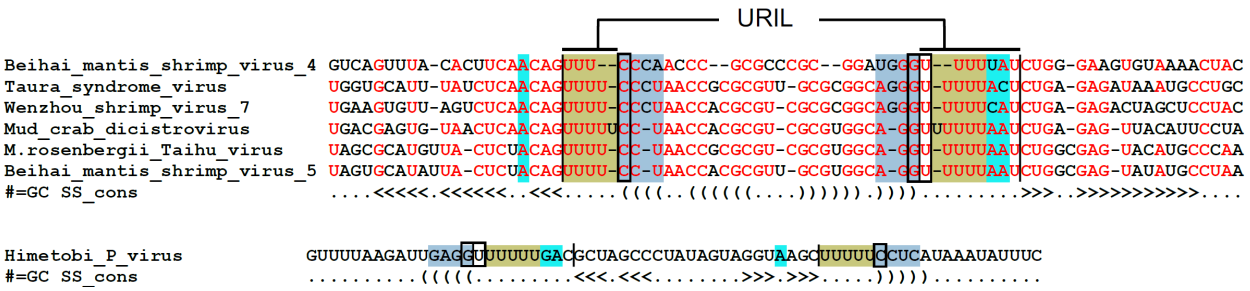

Fig. S25. Secondary structure-guided alignment of viral single-domain ENE sequences containing a putative poly(A) 3′-end binding pocket. Note that all of these ENEs are found in positive-sense RNA viruses. The Himetobi P virus ENE appears in inverted orientation relative to the other ENEs. Residues putatively involved in the quintuple-base transition are boxed, while those constituting the adenosine triad, which is involved in poly(A) 3′-end binding pocket formation, are shaded in cyan. The U residues involved in predicted U-A•U triple-helix formation in ENE are shaded green, while pyrimidine/purine (Y/R) biased stems are shaded blue. The red residues in the upper panel are at least 60% conserved.

Table S1. Crystallographic data collection and refinement statistics.

	Native	Iridium derivative		
Data collection				
Space group	$P6_422$		$P6_422$	
Cell dimensions				
a, b, c (Å)	93.9, 93.9, 202.2		95.5, 95.5, 206.1	
α, β, γ (°)	90.0, 90.0, 120.0		90.0, 90.0, 120.0	
		Peak	*Inflection*	*Remote*
Wavelength	0.9792	1.1053	1.1060	1.1046
Resolution	46.99 - 2.89 (2.99 - 2.89)[a]	100.00 - 3.00 (3.05 - 3.00)	100.00 - 3.00 (3.05 - 3.00)	100.00 - 3.00 (3.05 - 3.00)
Total reflections	194340 (8265)	226494	229357	177161
Unique reflections	11859 (812)	12211	12313	9607
Completeness (%)	95.1 (67.3)	99.9	99.9	99.9
Redundancy	16.4 (10.2)	10.3 (10.2)	10.4 (10.3)	10.4 (8.9)
Mean $I / \sigma I$	17.1 (0.66)[b]	20.4 (0.48)[b]	18.2 (0.30)[b]	14.4 (0.30)[b]
R_{merge}	0.147 (3.293)	0.17	0.16	0.21
R_{meas}	0.151 (3.45)	0.18	0.16	0.27
R_{pim}	0.0374 (0.979)	0.057	0.049	0.095
$CC_{1/2}$ (*74*)	0.994 (0.199)	0.99 (0.15)	0.99 (0.11)	0.99 (0.10)
CC* (*75*)	0.998 (0.576)	1.00 (0.51)	1.00 (0.45)	1.00 (0.43)
Refinement				
Resolution (Å)	46.99 - 2.89			
No. reflections	11849 (812)			
R_{work} / R_{free}	0.184 / 0.225			
No. atoms	2445			
Macromolecule	2301			
Ligand/ion	144			
B-factor (Å^2)	115.7			
Macromolecule	113.6			
Ligand/ion	148.7			
r.m.s. deviations				
Bond lengths (Å)	0.009			
Bond angles (°)	1.87			

[a] Each dataset was collected from a single crystal. Values in parentheses are for highest resolution shell.

[b] $I / \sigma I = 2$ at 3.18 Å, 3.23 Å, 3.30 Å, 3.30 Å

References

1. J. V. Geisberg, Z. Moqtaderi, X. Fan, F. Ozsolak, K. Struhl, Global analysis of mRNA isoform half-lives reveals stabilizing and destabilizing elements in yeast. *Cell* **156**, 812–824 (2014). doi:10.1016/j.cell.2013.12.026 Medline

2. M. Kim, N. Kogan, F. J. Slack, Cis-acting elements in its 3′ UTR mediate post-transcriptional regulation of KRAS. *Oncotarget* **7**, 11770–11784 (2016). doi:10.18632/oncotarget.7599 Medline

3. O. Mizrahi, A. Nachshon, A. Shitrit, I. A. Gelbart, M. Dobesova, S. Brenner, C. Kahana, N. Stern-Ginossar, Virus-induced changes in mRNA secondary structure uncover cis-regulatory elements that directly control gene expression. *Mol. Cell* **72**, 862–874.e5 (2018). doi:10.1016/j.molcel.2018.09.003

4. C. E. Vejnar, M. Abdel Messih, C. M. Takacs, V. Yartseva, P. Oikonomou, R. Christiano, M. Stoeckius, S. Lau, M. T. Lee, J.-D. Beaudoin, D. Musaev, H. Darwich-Codore, T. C. Walther, S. Tavazoie, D. Cifuentes, A. J. Giraldez, Genome wide analysis of 3′ UTR sequence elements and proteins regulating mRNA stability during maternal-to-zygotic transition in zebrafish. *Genome Res.* **29**, 1100–1114 (2019). doi:10.1101/gr.245159.118 Medline

5. B. M. Akiyama, D. Eiler, J. S. Kieft, Structured RNAs that evade or confound exonucleases: Function follows form. *Curr. Opin. Struct. Biol.* **36**, 40–47 (2016). doi:10.1016/j.sbi.2015.12.006 Medline

6. N. K. Conrad, J. A. Steitz, A Kaposi's sarcoma virus RNA element that increases the nuclear abundance of intronless transcripts. *EMBO J.* **24**, 1831–1841 (2005). doi:10.1038/sj.emboj.7600662 Medline

7. J. A. Brown, M. L. Valenstein, T. A. Yario, K. T. Tycowski, J. A. Steitz, Formation of triple-helical structures by the 3′-end sequences of MALAT1 and MENβ noncoding RNAs. *Proc. Natl. Acad. Sci. U.S.A.* **109**, 19202–19207 (2012). doi:10.1073/pnas.1217338109 Medline

8. J. E. Wilusz, C. K. JnBaptiste, L. Y. Lu, C.-D. Kuhn, L. Joshua-Tor, P. A. Sharp, A triple helix stabilizes the 3′ ends of long noncoding RNAs that lack poly(A) tails. *Genes Dev.* **26**, 2392–2407 (2012). doi:10.1101/gad.204438.112 Medline

9. K. T. Tycowski, M. D. Shu, J. A. Steitz, Myriad triple-helix-forming structures in the transposable element RNAs of plants and fungi. *Cell Rep.* **15**, 1266–1276 (2016). doi:10.1016/j.celrep.2016.04.010 Medline

10. N. K. Conrad, S. Mili, E. L. Marshall, M. D. Shu, J. A. Steitz, Identification of a rapid mammalian deadenylation-dependent decay pathway and its inhibition by a viral RNA element. *Mol. Cell* **24**, 943–953 (2006). doi:10.1016/j.molcel.2006.10.029 Medline

11. R. M. Mitton-Fry, S. J. DeGregorio, J. Wang, T. A. Steitz, J. A. Steitz, Poly(A) tail recognition by a viral RNA element through assembly of a triple helix. *Science* **330**, 1244–1247 (2010). doi:10.1126/science.1195858 Medline

12. N. K. Conrad, M. D. Shu, K. E. Uyhazi, J. A. Steitz, Mutational analysis of a viral RNA element that counteracts rapid RNA decay by interaction with the polyadenylate tail. *Proc. Natl. Acad. Sci. U.S.A.* **104**, 10412–10417 (2007). doi:10.1073/pnas.0704187104 Medline

13. S. Borah, N. Darricarrère, A. Darnell, J. Myoung, J. A. Steitz, A viral nuclear noncoding RNA binds re-localized poly(A) binding protein and is required for late KSHV gene expression. *PLOS Pathog.* **7**, e1002300 (2011). doi:10.1371/journal.ppat.1002300 Medline

14. K. T. Tycowski, M. D. Shu, S. Borah, M. Shi, J. A. Steitz, Conservation of a triple-helix-forming RNA stability element in noncoding and genomic RNAs of diverse viruses. *Cell Rep.* **2**, 26–32 (2012). doi:10.1016/j.celrep.2012.05.020 Medline

15. T. Gutschner, M. Hämmerle, S. Diederichs, MALAT1—A paradigm for long noncoding RNA function in cancer. *J. Mol. Med.* **91**, 791–801 (2013). doi:10.1007/s00109-013-1028-y Medline

16. S. Dhamija, S. Diederichs, From junk to master regulators of invasion: lncRNA functions in migration, EMT and metastasis. *Int. J. Cancer* **139**, 269–280 (2016). doi:10.1002/ijc.30039 Medline

17. J. A. Brown, D. Bulkley, J. Wang, M. L. Valenstein, T. A. Yario, T. A. Steitz, J. A. Steitz, Structural insights into the stabilization of MALAT1 noncoding RNA by a bipartite triple helix. *Nat. Struct. Mol. Biol.* **21**, 633–640 (2014). doi:10.1038/nsmb.2844 Medline

18. P. Nissen, J. A. Ippolito, N. Ban, P. B. Moore, T. A. Steitz, RNA tertiary interactions in the large ribosomal subunit: The A-minor motif. *Proc. Natl. Acad. Sci. U.S.A.* **98**, 4899–4903 (2001). doi:10.1073/pnas.081082398 Medline

19. J. A. Brown, Unraveling the structure and biological functions of RNA triple helices. *Wiley Interdiscip. Rev. RNA* **11**, e1598 (2020). doi:10.1002/wrna.1598 Medline

20. A. L. Edwards, F. E. Reyes, A. Héroux, R. T. Batey, Structural basis for recognition of S-adenosylhomocysteine by riboswitches. *RNA* **16**, 2144–2155 (2010). doi:10.1261/rna.2341610 Medline

21. M. Yamada, Y. Watanabe, J. S. Gootenberg, H. Hirano, F. A. Ran, T. Nakane, R. Ishitani, F. Zhang, H. Nishimasu, O. Nureki, Crystal structure of the minimal Cas9 from campylobacter jejuni reveals the molecular diversity in the CRISPR-Cas9 systems. *Mol. Cell* **65**, 1109–1121.e3 (2017). doi:10.1016/j.molcel.2017.02.007 Medline

22. N. K. Kim, Q. Zhang, J. Zhou, C. A. Theimer, R. D. Peterson, J. Feigon, Solution structure and dynamics of the wild-type pseudoknot of human telomerase RNA. *J. Mol. Biol.* **384**, 1249–1261 (2008). doi:10.1016/j.jmb.2008.10.005 Medline

23. S. D. Gilbert, R. P. Rambo, D. Van Tyne, R. T. Batey, Structure of the SAM-II riboswitch bound to S-adenosylmethionine. *Nat. Struct. Mol. Biol.* **15**, 177–182 (2008). doi:10.1038/nsmb.1371 Medline

24. D. J. Klein, T. E. Edwards, A. R. Ferré-D'Amaré, Cocrystal structure of a class I preQ1 riboswitch reveals a pseudoknot recognizing an essential hypermodified nucleobase. *Nat. Struct. Mol. Biol.* **16**, 343–344 (2009). doi:10.1038/nsmb.1563 Medline

25. J. A. Liberman, K. C. Suddala, A. Aytenfisu, D. Chan, I. A. Belashov, M. Salim, D. H. Mathews, R. C. Spitale, N. G. Walter, J. E. Wedekind, Structural analysis of a class III preQ1 riboswitch reveals an aptamer distant from a ribosome-binding site regulated by fast dynamics. *Proc. Natl. Acad. Sci. U.S.A.* **112**, E3485–E3494 (2015). doi:10.1073/pnas.1503955112 Medline

26. M. Kang, R. Peterson, J. Feigon, Structural Insights into riboswitch control of the biosynthesis of queuosine, a modified nucleotide found in the anticodon of tRNA. *Mol. Cell* **33**, 784–790 (2009). doi:10.1016/j.molcel.2009.02.019 Medline

27. J. M. Molleston, S. Cherry, Attacked from all sides: RNA decay in antiviral defense. *Viruses* **9**, 2 (2017). doi:10.3390/v9010002 Medline

28. J. Yeo, V. N. Kim, U-tail as a guardian against invading RNAs. *Nat. Struct. Mol. Biol.* **25**, 903–905 (2018). doi:10.1038/s41594-018-0139-0 Medline

29. J. C. Zinder, C. D. Lima, Targeting RNA for processing or destruction by the eukaryotic RNA exosome and its cofactors. *Genes Dev.* **31**, 88–100 (2017). doi:10.1101/gad.294769.116 Medline

30. Z. Warkocki, P. S. Krawczyk, D. Adamska, K. Bijata, J. L. Garcia-Perez, A. Dziembowski, Uridylation by TUT4/7 restricts retrotransposition of human LINE-1s. *Cell* **174**, 1537–1548.e29 (2018). doi:10.1016/j.cell.2018.07.022 Medline

31. J. Le Pen, H. Jiang, T. Di Domenico, E. Kneuss, J. Kosałka, C. Leung, M. Morgan, C. Much, K. L. M. Rudolph, A. J. Enright, D. O'Carroll, D. Wang, E. A. Miska, Terminal uridylyltransferases target RNA viruses as part of the innate immune system. *Nat. Struct. Mol. Biol.* **25**, 778–786 (2018). doi:10.1038/s41594-018-0106-9 Medline

32. Z. Moqtaderi, J. V. Geisberg, K. Struhl, Secondary structures involving the poly(A) tail and other 3′ sequences are major determinants of mRNA isoform stability in yeast. *Microb. Cell* **1**, 137–139 (2014). doi:10.15698/mic2014.04.140 Medline

33. X. Wu, D. P. Bartel, Widespread influence of 3′-end structures on mammalian mRNA processing and stability. *Cell* **169**, 905–917.e11 (2017). doi:10.1016/j.cell.2017.04.036 Medline

34. I. B. Schäfer, M. Yamashita, J. M. Schuller, S. Schüssler, P. Reichelt, M. Strauss, E. Conti, Molecular basis for poly(A) RNP architecture and recognition by the Pan2-Pan3 deadenylase. *Cell* **177**, 1619–1631.e21 (2019). doi:10.1016/j.cell.2019.04.013 Medline

35. C. P. Wigington, K. R. Williams, M. P. Meers, G. J. Bassell, A. H. Corbett, Poly(A) RNA-binding proteins and polyadenosine RNA: New members and novel functions. *Wiley Interdiscip. Rev. RNA* **5**, 601–622 (2014). doi:10.1002/wrna.1233 Medline

36. J. M. Avis, G. L. Conn, S. C. Walker, Cis-acting ribozymes for the production of RNA in vitro transcripts with defined 5′ and 3′ ends. *Methods Mol. Biol.* **941**, 83–98 (2012). doi:10.1007/978-1-62703-113-4_7 Medline

37. B. L. Golden, C. E. Kundrot, RNA crystallization. *J. Struct. Biol.* **142**, 98–107 (2003). doi:10.1016/S1047-8477(03)00042-X Medline

38. W. Kabsch, Xds. *Acta Crystallogr. D* **66**, 125–132 (2010). doi:10.1107/S0907444909047337 Medline

39. Z. Otwinowski, W. Minor, Processing of X-ray diffraction data collected in oscillation mode. *Methods Enzymol.* **276**, 307–326 (1997). doi:10.1016/S0076-6879(97)76066-X

40. G. M. Sheldrick, Experimental phasing with SHELXC/D/E: Combining chain tracing with density modification. *Acta Crystallogr. D* **66**, 479–485 (2010). doi:10.1107/S0907444909038360 Medline

41. A. J. McCoy, R. W. Grosse-Kunstleve, P. D. Adams, M. D. Winn, L. C. Storoni, R. J. Read, Phaser crystallographic software. *J. Appl. Crystallogr.* **40**, 658–674 (2007). doi:10.1107/S0021889807021206 Medline

42. M. D. Winn, C. C. Ballard, K. D. Cowtan, E. J. Dodson, P. Emsley, P. R. Evans, R. M. Keegan, E. B. Krissinel, A. G. W. Leslie, A. McCoy, S. J. McNicholas, G. N. Murshudov, N. S. Pannu, E. A. Potterton, H. R. Powell, R. J. Read, A. Vagin, K. S. Wilson, Overview of the CCP4 suite and current developments. *Acta Crystallogr. D* **67**, 235–242 (2011). doi:10.1107/S0907444910045749 Medline

43. P. Emsley, B. Lohkamp, W. G. Scott, K. Cowtan, Features and development of Coot. *Acta Crystallogr. D* **66**, 486–501 (2010). doi:10.1107/S0907444910007493 Medline

44. G. N. Murshudov, A. A. Vagin, E. J. Dodson, Refinement of macromolecular structures by the maximum-likelihood method. *Acta Crystallogr. D* **53**, 240–255 (1997). doi:10.1107/S0907444996012255 Medline

45. L. P. Ford, J. Watson, J. D. Keene, J. Wilusz, ELAV proteins stabilize deadenylated intermediates in a novel in vitro mRNA deadenylation/degradation system. *Genes Dev.* **13**, 188–201 (1999). doi:10.1101/gad.13.2.188 Medline

46. A. L. Fuchs, A. Neu, R. Sprangers, A general method for rapid and cost-efficient large-scale production of 5′ capped RNA. *RNA* **22**, 1454–1466 (2016). doi:10.1261/rna.056614.116 Medline

47. J. D. Dignam, R. M. Lebovitz, R. G. Roeder, Accurate transcription initiation by RNA polymerase II in a soluble extract from isolated mammalian nuclei. *Nucleic Acids Res.* **11**, 1475–1489 (1983). doi:10.1093/nar/11.5.1475 Medline

48. N. B. Leontis, E. Westhof, Geometric nomenclature and classification of RNA base pairs. *RNA* **7**, 499–512 (2001). doi:10.1017/S1355838201002515 Medline

49. R. M. Bock, Controlled partial hydrolysis of RNA. *Methods Enzymol.* **12**, 218–221 (1967). doi:10.1016/S0076-6879(67)12033-8

50. G. P. Pijlman, A. Funk, N. Kondratieva, J. Leung, S. Torres, L. van der Aa, W. J. Liu, A. C. Palmenberg, P.-Y. Shi, R. A. Hall, A. A. Khromykh, A highly structured, nuclease-resistant, noncoding RNA produced by flaviviruses is required for pathogenicity. *Cell Host Microbe* **4**, 579–591 (2008). doi:10.1016/j.chom.2008.10.007 Medline

51. R. Rauhut, G. Klug, mRNA degradation in bacteria. *FEMS Microbiol. Rev.* **23**, 353–370 (1999). doi:10.1111/j.1574-6976.1999.tb00404.x Medline

52. B. M. Akiyama, H. M. Laurence, A. R. Massey, D. A. Costantino, X. Xie, Y. Yang, P.-Y. Shi, J. C. Nix, J. D. Beckham, J. S. Kieft, Zika virus produces noncoding RNAs using a multi-pseudoknot structure that confounds a cellular exonuclease. *Science* **354**, 1148–1152 (2016). doi:10.1126/science.aah3963 Medline

53. A. L. Steckelberg, B. M. Akiyama, D. A. Costantino, T. L. Sit, J. C. Nix, J. S. Kieft, A folded viral noncoding RNA blocks host cell exoribonucleases through a conformationally dynamic RNA structure. *Proc. Natl. Acad. Sci. U.S.A.* **115**, 6404–6409 (2018). doi:10.1073/pnas.1802429115 Medline

54. A. L. Steckelberg, Q. Vicens, D. A. Costantino, J. C. Nix, J. S. Kieft, The crystal structure of a Polerovirus exoribonuclease-resistant RNA shows how diverse sequences are integrated into a conserved fold. *RNA* **26**, 1767–1776 (2020). doi:10.1261/rna.076224.120 Medline

55. S. Meyer, C. Temme, E. Wahle, Messenger RNA turnover in eukaryotes: Pathways and enzymes. *Crit. Rev. Biochem. Mol. Biol.* **39**, 197–216 (2004). doi:10.1080/10409230490513991 Medline

56. S. Yu, V. N. Kim, A tale of non-canonical tails: Gene regulation by post-transcriptional RNA tailing. *Nat. Rev. Mol. Cell Biol.* **21**, 542–556 (2020). doi:10.1038/s41580-020-0246-8 Medline

57. M. Lingaraju, J. M. Schuller, S. Falk, P. Gerlach, F. Bonneau, J. Basquin, C. Benda, E. Conti, To process or to decay: A mechanistic view of the nuclear RNA exosome. *Cold Spring Harb. Symp. Quant. Biol.* **84**, 155–163 (2019). doi:10.1101/sqb.2019.84.040295 Medline

58. E. V. Wasmuth, K. Januszyk, C. D. Lima, Structure of an Rrp6-RNA exosome complex bound to poly(A) RNA. *Nature* **511**, 435–439 (2014). doi:10.1038/nature13406 Medline

59. J. C. Zinder, E. V. Wasmuth, C. D. Lima, Nuclear RNA exosome at 3.1 A reveals substrate specificities, RNA paths, and allosteric inhibition of Rrp44/Dis3. *Mol. Cell* **64**, 734–745 (2016). doi:10.1016/j.molcel.2016.09.038 Medline

60. W. K. Olson, S. Li, T. Kaukonen, A. V. Colasanti, Y. Xin, X.-J. Lu, Effects of noncanonical base pairing on RNA folding: Structural context and spatial arrangements of G·A Pairs. *Biochemistry* **58**, 2474–2487 (2019). doi:10.1021/acs.biochem.9b00122 Medline

61. D. J. Proctor, H. Ma, E. Kierzek, R. Kierzek, M. Gruebele, P. C. Bevilacqua, Folding thermodynamics and kinetics of YNMG RNA hairpins: Specific incorporation of 8-bromoguanosine leads to stabilization by enhancement of the folding rate. *Biochemistry* **43**, 14004–14014 (2004). doi:10.1021/bi048213e Medline

62. K. B. Hall, Mighty tiny. *RNA* **21**, 630–631 (2015). doi:10.1261/rna.050567.115 Medline

63. D. J. Battle, J. A. Doudna, Specificity of RNA-RNA helix recognition. *Proc. Natl. Acad. Sci. U.S.A.* **99**, 11676–11681 (2002). doi:10.1073/pnas.182221799 Medline

64. A. Lescoute, E. Westhof, The A-minor motifs in the decoding recognition process. *Biochimie* **88**, 993–999 (2006). doi:10.1016/j.biochi.2006.05.018 Medline

65. Y. Xin, C. Laing, N. B. Leontis, T. Schlick, Annotation of tertiary interactions in RNA structures reveals variations and correlations. *RNA* **14**, 2465–2477 (2008). doi:10.1261/rna.1249208 Medline

66. L. Wu, D. Chai, M. E. Fraser, S. Zimmerly, Structural variation and uniformity among tetraloop-receptor interactions and other loop-helix interactions in RNA crystal structures. *PLOS ONE* **7**, e49225 (2012). doi:10.1371/journal.pone.0049225 Medline

67. L. D'Ascenzo, Q. Vicens, P. Auffinger, Identification of receptors for UNCG and GNRA Z-turns and their occurrence in rRNA. *Nucleic Acids Res.* **46**, 7989–7997 (2018). doi:10.1093/nar/gky578 Medline

68. C. Bou-Nader, J. Zhang, Structural insights into RNA dimerization: Motifs, interfaces and functions. *Molecules* **25**, 2881 (2020). doi:10.3390/molecules25122881 Medline

69. S. L. Vi, G. Trost, P. Lange, H. Czesnick, N. Rao, D. Lieber, T. Laux, W. M. Gray, J. L. Manley, D. Groth, C. Kappel, M. Lenhard, Target specificity among canonical nuclear poly(A) polymerases in plants modulates organ growth and pathogen response. *Proc. Natl. Acad. Sci. U.S.A.* **110**, 13994–13999 (2013). doi:10.1073/pnas.1303967110 Medline

70. L. Minvielle-Sebastia, P. J. Preker, T. Wiederkehr, Y. Strahm, W. Keller, The major yeast poly(A)-binding protein is associated with cleavage factor IA and functions in premessenger RNA 3′-end formation. *Proc. Natl. Acad. Sci. U.S.A.* **94**, 7897–7902 (1997). doi:10.1073/pnas.94.15.7897 Medline

71. A. O. Subtelny, S. W. Eichhorn, G. R. Chen, H. Sive, D. P. Bartel, Poly(A)-tail profiling reveals an embryonic switch in translational control. *Nature* **508**, 66–71 (2014). doi:10.1038/nature13007 Medline

72. H. Chang, J. Lim, M. Ha, V. N. Kim, TAIL-seq: Genome-wide determination of poly(A) tail length and 3′ end modifications. *Mol. Cell* **53**, 1044–1052 (2014). doi:10.1016/j.molcel.2014.02.007 Medline

73. D. P. Giedroc, P. V. Cornish, Frameshifting RNA pseudoknots: Structure and mechanism. *Virus Res.* **139**, 193–208 (2009). doi:10.1016/j.virusres.2008.06.008 Medline

74. P. A. Karplus, K. Diederichs, Linking crystallographic model and data quality. *Science* **336**, 1030–1033 (2012). doi:10.1126/science.1218231 Medline

75. P. A. Karplus, K. Diederichs, Assessing and maximizing data quality in macromolecular crystallography. *Curr. Opin. Struct. Biol.* **34**, 60–68 (2015). doi:10.1016/j.sbi.2015.07.003 Medline